Daniela Edlinger, BSc

Sensing of Carbon Dioxide Concentration in Exhaled Air via Thermal Conductivity Measurement

MASTER'S THESIS

to achieve the university degree of

Diplom-Ingenieurin

Master's degree programme: Biomedical Engineering

submitted to

Graz University of Technology

Supervisors

Ao.Univ.-Prof. Dipl.-Ing. Dr. techn. Hermann Scharfetter
Institute of Biomedical Imaging
Stremayrgasse 16/III

Dipl.-Ing. Dr.techn. Christoph Steiner
Infineon Technologies Austria AG
Babenbergerstraße 10

Graz, May 2024

AFFIDAVIT

I declare that I have authored this thesis independently, that I have not used other than the declared sources/resources, and that I have explicitly indicated all material which has been quoted either literally or by content from the sources used. The text document uploaded to TUGRAZonline is identical to the present master's thesis.

....

Date Signature

Acknowledgements

First and foremost, I would like to express my gratitude to my supervisor, Dipl.-Ing. Dr. techn. Christoph Steiner, for making this thesis in cooperation with Infineon even possible. I am very thankful for his invaluable support throughout this thesis. His ideas and contribution helped me a lot completing this thesis. I would also like to thank Ao. Univ.-Prof. Dipl.-Ing. Dr. techn. Hermann Scharfetter for his expertise, feedback and supervision.

Furthermore, I would like to thank my colleague Johannes Hufnagl. He provided invaluable advice and guidance throughout the thesis, supporting me whenever it was needed. He was always there to listen to me, whether it was in a work related or personal manner.

I am also grateful to my colleagues and friends Alice and Sophia. They made every day at work special with their presence. Thank you for always cheering me up and providing me with great input throughout my thesis.

I would also like to thank my parents, Peter and Eveline, for their financial support and for providing me with the opportunity to pursue my studies. I would also like to express my gratitude to my twin sister, Maria, for her unwavering support. She has always been there for me, and I know I can always count on her.

Finally, I would like to thank my friends who have had a significant impact on my life during my time in Graz and throughout my studies. You made my time here and during my studies really specially and I look back on it very gratefully.

Abstract

Thermal conductivity sensors have a wide range of applications, yet their potential use in health related fields, such as capnography, has been subject to limited investigation. Hence, a thermal conductivity sensor was used to measure the dynamic carbon dioxide curve during exhalation. To achieve this, a suitable measurement method was chosen. The sensitivity to carbon dioxide, as well as its cross sensitivities to humidity and temperature, were determined. By compensating for these cross sensitivities using a post processing algorithm, initial measurements were carried out successfully, demonstrating the suitability of this sensor principle in detecting carbon dioxide in exhaled breath. This provides a low cost, small size and fast alternative to the carbon dioxide sensors currently used in biomedical applications.

Keywords: thermal conductivity sensor, carbon dioxide sensor, capnography, gas sensor, CO_2

Kurzfassung

Wärmeleitfähigkeitssensoren sind vielseitig einsetzbar, jedoch gibt es nur wenige Untersuchungen zu ihrem Einsatz in medizinischen Anwendungen, wie beispielsweise der Kapnographie. Daher wurde ein Wärmeleitfähigkeitssensor zur Messung der dynamischen Kohlenstoffdioxidkurve während des Ausatmens entwickelt. Hierfür wurde eine geeignete Messmethode ausgewählt und die Empfindlichkeit gegenüber Kohlenstoffdioxid bestimmt. Ebenso wurde die Querempfindlichkeiten gegenüber Feuchtigkeit und Temperatur bestimmt. Durch die Kompensation von Querempfindlichkeiten in einem Nachbearbeitungsalgorithmus konnten erste Messungen durchgeführt werden und die Eignung dieses Sensorprinzips zur Detektion von Kohlenstoffdioxid in der Ausatemluft belegt werden. Somit bietet dieses Sensorprinzip eine kostengünstige, kompakte und schnelle Alternative zu den derzeit in biomedizinischen Anwendungen verwendeten Kohlenstoffdioxidsensoren.

Schlüsselwörter: Wärmeleitfähigkeitssensoren, Kohlenstoffdioxidsensoren, Kapnographie, Gassensor, CO_2

Contents

List of Figures

List of Tables

Abbreviations

CO_2 Carbon Dioxide

COPD Chronic Obstructive Pulmonary Disease

O_2 Oxygen

$petCO_2$ Partial Pressure of End-Tidal Carbon Dioxide

$paCO_2$ Carbon Dioxide Partial Pressure of Aterial Blood

IR Infrared

NDIR Non-Dispersive Infrared

$etCO_2$ End-Tidal Carbon Dioxide

PAS Photoacoustic Spectroscopy

H_2 Hydrogen

N_2 Nitrogen

TC sensor Thermal Conductivity Sensor

SMU Single Measurement Unit

RMS Root-Mean-Square

GUI Graphical User Interface

PCB Printed Circuit Board

I2C Inter-Integrated Circuit

ADC Analog-to-Digital Converter

MEIF Measurement Interface

UART Universal Asynchronous Receiver

SNR Signal-to-Noise Ratio

1 Introduction

Carbon dioxide (CO_2) sensing has numerous applications in various fields, including food storage, agriculture, and medicine [1]. In medicine, the concentration of CO_2 in exhaled air is an important diagnostic quantity [2]. The measurement of CO_2 enables non-invasive diagnosis of asthma, chronic obstructive pulmonary disease (COPD), and cardiovascular diseases [3]. As many health issues are linked to the level of exhaled CO_2, it is crucial to have a quick and precise method of detection [4].

A capnopraph is commonly used for this purpose. As these devices are very expensive, their usage is limited [5]. Here, the sensor principle currently used is infrared sensing. These sensors are expensive and add cost to the device. Additionally, they are also sensitive to humidity, which is present in exhaled air [3]. Therefore, there is a requirement for an affordable and concise substitute [5].

Thermal conductivity sensors may be a suitable alternative due to their wide measurement range, fast response time, and good long-term stability [6]. Kliche et al. [2] and Berndt et al. [6] suggested using thermal conductivity sensors to detect CO_2 in human breath. However, they both noted that the first step is to address the issue of fluctuating temperature and humidity in the breath, as this greatly affects the output of the thermal conductivity sensor. If these problems can be overcome, a low cost, wearable device could be a feasible option [2].

As there are only a few investigations in literature on the use of a thermal conductivity sensor for breath analysis, there is great motivation to invest further in this area. The aim of this thesis is to conduct a feasibility study on using thermal conductivity for sensing CO_2 concentration in exhaled air. Two different transient measurement methods, the pulsed hot wire method and the 3 omega method, were investigated to determine which one is more suitable to meet the desired specifications. As previously stated, a significant concern for using thermal conductivity sensors for capnography is the fluctuating temperature and humidity levels in exhaled breath. Both factors affect the output of the sensor and therefore require compensation. To achieve this, additional humidity and temperature sensors are utilized. The parasitic effects are algorithmically compensated in software during post-processing. To confirm that the thermal conductivity sensor used is suitable for breath analysis, different breathing techniques are used to validate that the sensor is responding in the correct way. If this is achieved successfully, a fast, low-cost, and miniaturizable alternative can be obtained.

1.1 Respiratory System

The respiratory system is responsible for the removal of CO_2 from the body by exhalation and the supply of oxygen (O_2) to the blood by inhalation. The inhaled air travels through all parts of the respiratory system until it reaches the alveoli, the smallest unit of the system. There the gas exchange takes place [7]. A more detailed structure of the respiratory system and the physiology of the gas exchange is provided in the following sections.

1.1.1 Anatomy

The respiratory system comprises of two parts: the upper respiratory tract and the the lower respiratory tract. The upper respiratory system includes the nose, the pharynx and the larynx [8]. The role of the nose is to filter, moisturise and heat the inhaled air. The air first passes through the nose and the nasal cavity before reaching the pharynx, which is a part of both the respiratory and digestive systems. Also in this region, the air is humidified and warmed up. The final segment of the upper respiratory tract is the larynx, commonly referred to as the voice box of the body, responsible for sound production. The epiglottis is a part of the larynx that closes over the larynx during swallowing to protect the lower respiratory tract [9].
The lower respiratory tract is comprised of the trachea, both bronchi, which then extend into the bronchioles, alveolar ducts and alveoli [8]. An overview of the upper and lower respiratory system is shown in the Figure 1.

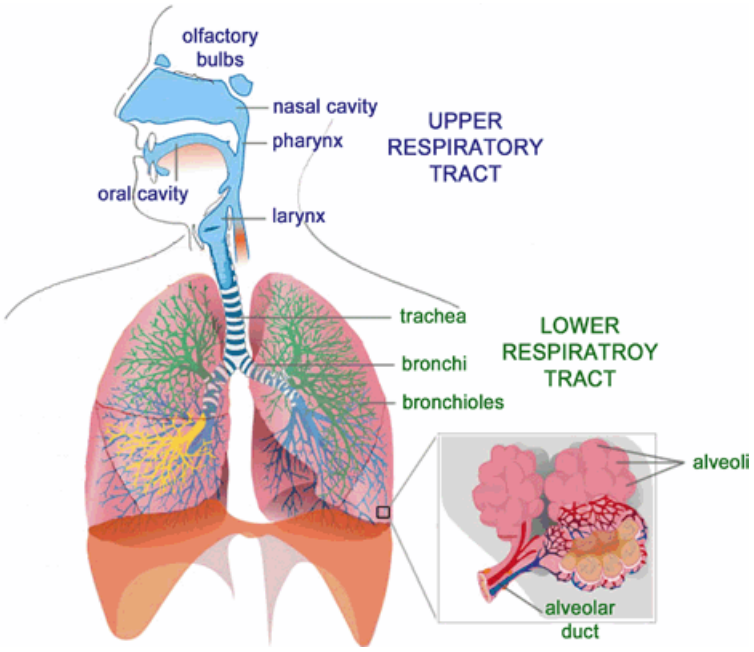

Figure 1: An Overview of the respiratory system. The upper respiratory tract includes the nose, nasal cavity, pharynx and larynx. The lower respiratory tract consists of trachea, bronchi, bronchioles, alveolar ducts and alveoli. Source: [10]

The first part of the lower respiratory tract, known as trachea, bifurcates into the right and left bronchi [8]. Each bronchus leads to one of the two lungs. The right lung is made up of three lobes, while the left lung has only two lobes. The smaller size of the left lung is due to the extra space required by the heart. The pleura is a double-layered membrane that surrounds the lungs. The inner layer covers the surface of the lungs, while the outer layer lines the inside of the chest wall. The space between these two layers is called the pleural cavity and is filled with a serous fluid [9].
The bronchi split into bronchioles and then further into alveolar ducts, which are lined with alveoli. The alveoli have a very small diameter of 0.25 mm, but since there are approximately 300 million alveoli in the respiratory zone, the total area is approximately 140 m^2. [7]
The region, reaching from the trachea to the terminal bronchioles, is called conducting zone. Gas exchange does not occur in this region, and therefore the volume is referred to as dead space volume, which contains approximately 150 ml. The remaining part of the respiratory system is called respiratory zone. This zone reaches from the respiratory bronchioles to the alveoli. [8]

1.1.2 Physiology

The lung is an assembly of alveoli in which gas exchange takes place between capillary blood and inhaled air. During gas exchange, venous blood becomes enriched with O_2 and CO_2 is removed [11]. The left ventricle of the heart pumps oxygenated blood through the circulatory system to peripheral tissues, where the mitochondria consume O_2 and produce CO_2. The blood, which is high in CO_2 and low in O_2 is subsequently pumped by the right ventricle from the peripheral veins to the lungs [12].
Boron [12] explains how the process of gas exchange in the lungs takes place. The main contributing factor here is a passive process known as diffusion. Diffusion is the net movement of molecules or substances from an area with high concentration to an area with low concentration. The concentration gradient during gas exchange results from partial pressure differences between the blood gases and the ambient air [12]. Partial pressure is the fraction of the total pressure produced by a single gas [9]. According to Henry's Law, the partial pressure is proportional to the concentration of a dissolved gas. Therefore, the partial pressure can take the place of concentration in Fick's 1^{st} diffusion law. Consequently, the net movement of particles is driven by the partial pressure difference [13].

Blood with a low partial pressure of oxygen is transported to the alveoli. In the alveolar gas the partial pressure of oxygen is much higher, therefore oxygen diffuses from the alveolar gas into the blood. For carbon dioxide the process is reversed. The blood in the capillaries surrounding the alveoli maintains a high partial pressure, while the alveolar gas has a low partial pressure [14]. This principle is also shown in the following Figure.

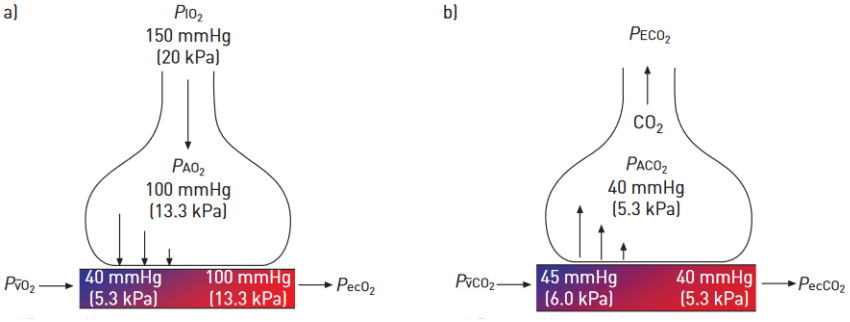

Figure 2: Overview of the partial pressure differences between capillary blood and alveolar gas. On the left the gas exchange of oxygen is shown, where oxygen diffuses from the alveolar gas into the blood to balance out the partial pressure difference. On the right side the exchange of carbon dioxide is shown. Here carbon dioxide diffuses from the blood to the alveolar gas. Source: [13]

1.1.3 Ventilation

During normal breathing, the two primary muscles involved are the intercostal muscles and the diaphragm. The intercostal muscles are located between the twelve ribs. The diaphragm muscle is dome-shaped and functions to separate the thorax from the abdomen. [9]

During breathing muscle contraction consume energy. Inhalation causes the thorax to expand due to the downward movement of the diaphragm. Simultaneously, the external intercostal muscles contract and raise the ribs, resulting in an elevation of the thoracic cavity. The increase in volume leads to a decrease in pressure within the thorax, compared to the atmospheric pressure. This pressure differential facilitates the movement of air into the lungs and alveoli. Upon exhaling, the diaphragm and intercostal muscles relax, causing the pressure in the thoracic cavity, which was present before inhalation, to return. This pressure is slightly higher than the atmospheric pressure, thereby inducing the exhalation of air. [7]

Table 1 lists the composition of inhaled and exhaled air, showing that the only components that change are oxygen and carbon dioxide. Typical values for CO_2 in adults range from 3.8% to 5.8%. The respiratory rate for an adult typically ranges from 12 to 20 breaths per minute. [15]

Table 1: Composition of inhaled and exhaled air. The only two components that change are oxygen and carbon dioxide. Source: [15]

Substance	Inhaled (%)	Exhaled (%)
Nitrogen	74	74
Oxygen	21	16
Carbon Dioxide	0.039	4
Argon	0.9	0.9

The exhaled breath is assumed to be 100% humidity. However, in practice, it is not expected to measure a value of 100% due to the air surrounding the humidity sensor having a different humidity level. The average temperature of exhaled breath is 34.5°C. [16]

1.2 Capnometery

Capnometry is the technique for monitoring CO_2 in the exhaled breath. The measurement includes the determination of the partial pressure of the end-tidal CO_2 value ($petCO_2$). In the absence of ventilation-perfusion mismatch or elevated dead space, the $petCO_2$ can be used as an approximation for the partial pressure of CO_2 in arterial blood $paCO_2$. However, this approximation is not possible under unstable haemodynamic conditions. Capnography refers to the plot of a capnogram, which is the partial pressure of CO_2 in the exhaled breath over time. A capnogram has diverse applications in medicine. It serves to monitor respiratory airflow and the production of CO_2, providing information about the quality of endotracheal intubation. Additionally, it can detect apnea, heart failure or COPD. [1]

1.2.1 Working Principle

The sensor principle commonly used in capnometry is based on the measurement of the infrared (IR) absorption of CO_2. There a two types of sensors available, either a non-dispersive infrared (NDIR) or a photoacoustic sensor is used [1]. A detailed explanation of these sensor principles is given in the section 1.3. The primary elements of a capnometer consist of an IR source, a sample cell and an IR radiation detector [17]. The gas molecules of CO_2 have a strong absorption at 4.26 μm. The concentration can then be further calculated with the Beer-Lambert law [5].

Two types of capnometer can be distinguished: the mainstream capnometer and the sidestream capnometer. Figure 3 provides an overview of these two types. In a mainstream capnometer the IR source and the detector are directly placed on opposite sides of the airway adapter and a cable transmits the measured signal to an external monitor. This method of measurement allows a real-time monitoring. The technique is constrained by its weight and size limitations, given that the increased mechanical dead space and issues of weight on the airway are problematic. Additionally, the presence of condensate in the sample cell can introduce additional scattering and absorption, which can distort the results. A sidestream capnometer aspirates a portion of the exhaled air and transports it through a small tube to the sensor. This transportation causes a delay time, thus the measurements are not in real time. Additionally, condensation and secretions have the potential to block the sampling tube. [17]

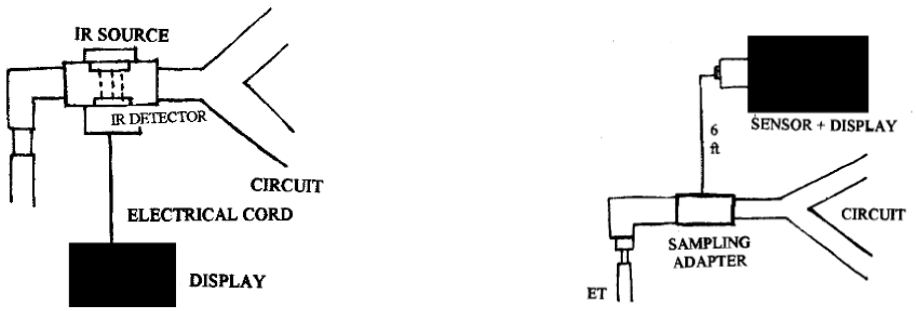

(a) Mainstream capnometer

(b) Sidestream Capnometer

Figure 3: Main components and structure of a mainstream and sidestream capnometer. Both types consist of a IR source, a detector and a sampling adapter. Mainstream capnometer have the IR source and the detector directly placed on opposite sides of the airway adapter. Sidestream capnometers analyse exhaled air using an external sensor, which requires aspirating a portion of the exhaled air. Source: [18]

The response time for a mainstream capnometer is over 50 ms. However, for a sidestream capnometer, the response time is longer due to the air having to pass through the tube. The added time is dependent on the suction flow, as well as the length and diameter of the tube [19]. The delay caused by that ranges from 1 to 4 seconds [20].

1.2.2 Capnography

As previously stated, a capnogram visualises the partial pressure of CO_2 over time. The resulting curve can be split into four different phases, as shown in Figure 4. A capnogram is divided into two parts, expiration and inspiration, the latter represented by Phase I. During this phase, the ambient air inhaled does not contain CO_2 and therefore the partial pressure of CO_2 is zero. Phase II, III, and IV belong to expiration [21]. Phase II is also missing CO_2 as it includes the air volume of the anatomical dead space [1]. During Phase III, there is an increase in CO_2 due to the exhalation not only of dead space air but also alveolar gas. The final phase, Phase IV, is the alveolar plateau, where the end of the phase represents the maximum value of CO_2 and is known as the end-tidal CO_2 ($etCO_2$) value [21].

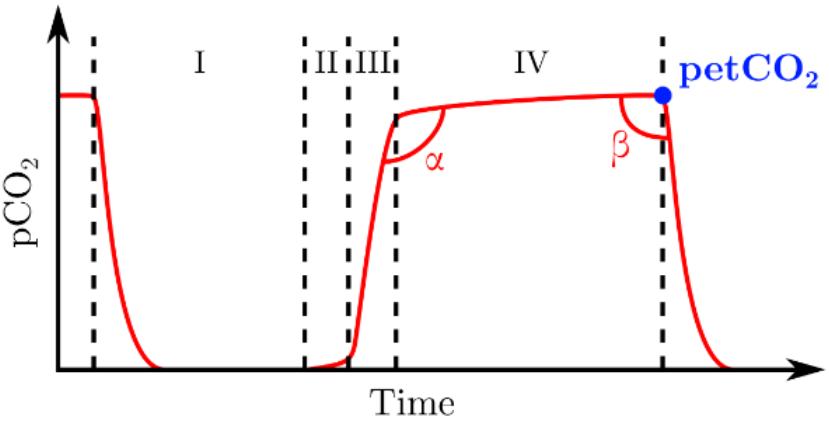

Figure 4: Four different phases of a capnogram. Phase I shows the inspiration, the Phases II, III and IV are part of the expiration. Phase II shows the CO_2 concentration of the dead space and Phase III a mixture out of alveolar and dead space air. The last Phase IV visualises the alveolar air. The endpoint of the plateau of Phase IV is called end-tidal CO_2 value. Source: [1]

In addition to the $etCO_2$ value, the capnogram contains two other important parameters, the alpha angle and the beta angle. The alpha angle is positioned between Phase III and Phase IV and typically ranges between 100° and 110°. An increased slope of Phase IV leads to a greater angle, which can indicate an airway obstruction. In Figure 5 an elevated alpha angle is demonstrated. The beta angle is between Phase IV and Phase I and has nearly 90°. An increase in the angle beta can indicate the extent of rebreathing. [18]

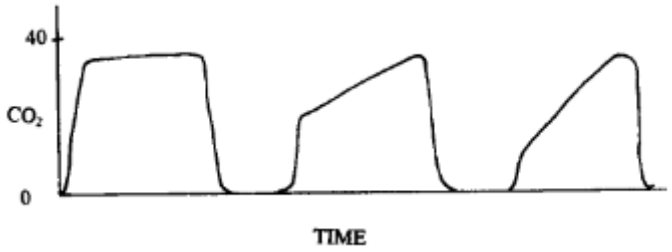

Figure 5: Increased slope of the alveolar plateau and consequently increased alpha angle indicates airway obstruction. Source: [18]

Typical values for $etCO_2$ are in the range of 35 mmHg and 40 mmHg. In healthy patients the $etCO_2$ value serves as an approximation of the arterial CO_2 value. The difference between these two values is about 3 to 5 mmHg [22]. Capnography can also detect respiratory system alterations, such as hyperventilation and hypoventilation. Here, the alveolar plateau persists whilst $etCO_2$ either decreases during hyperventilation, or increases during hypoventilation [18]. The according capnograms are shown in Figure 6.

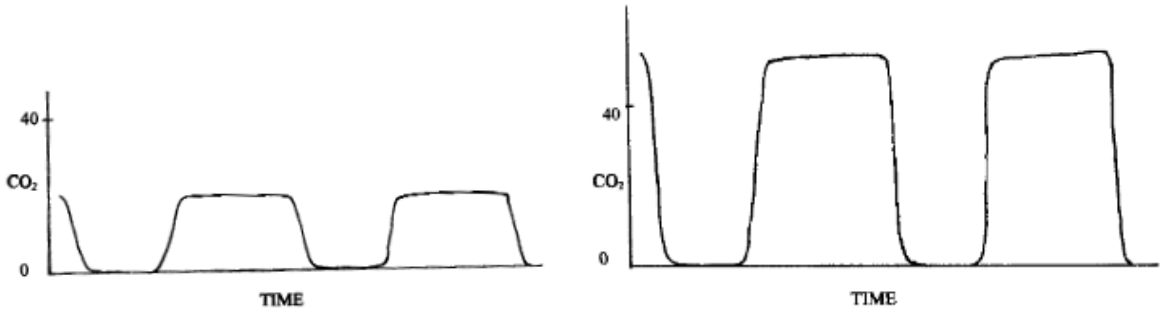

(a) Hyperventilation (b) Hypoventilation

Figure 6: Visualisation of hyperventilation and hypoventilation. In both cases the alveolar plateau remains the same but the $petCO_2$ decreases during hyperventilation and increases during hypoventilation. Source: [18]

The specifications for a capnometer are outlined in the ISO 21647, a standard discussing respiratory gas sensors. This standard defines the maximum level of inaccuracy according to Formula 1:

$$\pm\,(\text{volume fraction of } 0.43\% + 8\% \text{ of gas level}) \tag{1}$$

The standard reports the measurement range as 0 - 10% or 76 mmHg. Additionally, it specifies the permissible measurement drift. A capnograph shall not require a recalibration every few hours. [23]
The sampling time for capnographs typically ranges from 50 to 100 ms.

1.3 CO_2 sensors used in biomedical applications

There are various methods available for detecting CO_2, each with their own strengths and weaknesses. The forthcoming sections will detail these methods and evaluate their respective advantages and disadvantages. [1]

1.3.1 Non Dispersive Infrared (NDIR) Sensor

Non-dispersive infrared (NDIR) sensors are commonly used to measure CO_2 concentrations based on infrared absorption. The absorption band of CO_2 is at 4.26 μm. These sensors consist of a radiation source, sample cell, and detector, as illustrated in Figure 7. [17]

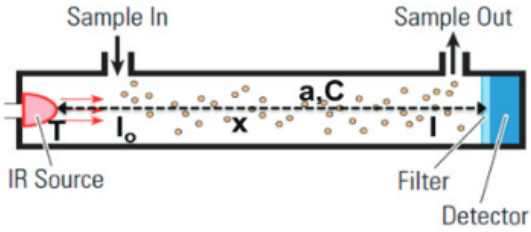

Figure 7: The basic components of a non dispersive infrared sensor are an IR source, a sample cell and a detector. The source emits light with the intensity I_0. The sample cell has the a certain length, containing the sample with an specific gas absorption coefficient and a concentration. The detector measures the remaining intensity I. Source: [5]

The intensity of radiation, measured by the detector, is depending on the concentration of the sample and the length of the sample cell. This is also stated in the Lambert-Beer law [17]. This law is represented in Formula 2:

$$I(\lambda) = I_0(\lambda)\, e^{-\alpha(\lambda)\, c\, l} \tag{2}$$

where $I_0(\lambda)$ refers to the emitted radiation, while $I(\lambda)$ denotes the measured radiation. The gas absorption coefficient, $\alpha(\lambda)$, depends on the wavelength of the IR signal emitted by the source. The remaining two parameters are c, the concentration, and l, the path length [24].

There are several IR sources that can be used for a NDIR system. These sources include micro bulbs, LEDs and MEMS IR sources [5]. Generally, an IR source must be able to emit a strong enough signal so that it can reach the detector. The source should also be able to emit the desired wavelength. Micro bulb lamps are favoured as IR source, as they are low cost, simple and have high spectral emissions [24]. The downsides of these lamps are their bulkiness, high power consumption, and reduced IR transmission efficiency due to the glass. LEDs have advantages like fast response time and a high optical output. However, similar to micro bulb lamps, LEDs also exhibit higher power consumption. Such

limitations can be overcome by using a MEMS IR source. As detector either thermopile or pyroelectric detectors are used [5].
The detection range goes from a few hundred ppm up to 100%. In order to measure small concentrations, a long light path is required, which can result in a bulky sensor.
NDIR sensors remain unaffected by humidity; however, water droplet formation within the sampling cell may lead to additional interferences. [1]

1.3.2 Photoacoustic Spectroscopy (PAS)

The main components of photoacoustic spectroscopy (PAS) are a radiation source, a sample cell and a detector to detect the acoustic signal. An overview of the schematic of a PAS is shown in Figure 8. The suitable light source requires modulation at high frequencies, which can be achieved using LEDs, pulsed lasers or even a continuous light source with a mechanical chopper [1]. The use of a light source necessitates the implementation of a filter to facilitate the extraction of the frequency band in which the absorption band of the gas to be sensed resides [25].

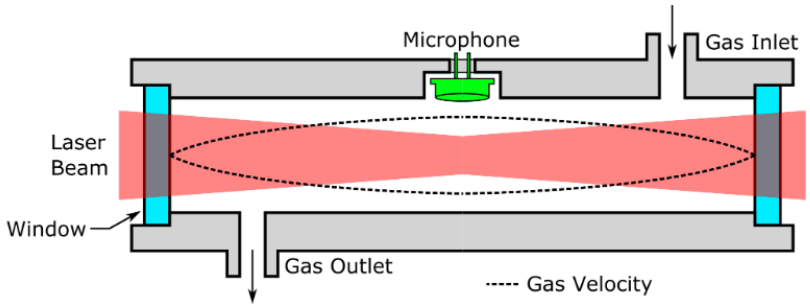

Figure 8: Structure of a photoacoustic spectroscopy. The main components are a light source, in this case a laser, a sample cell and a detector, for instant a microphone. The gas within the cell absorbs the emitted radiation and thus expanses. By turning off and on of the source, an acoustic wave is generated which is detected by the microphone. The amplitude of the signal is depending on the concentration of the gas sample. Source: [1]

The sensor principle is based on the absorption of photons of the radiation source, which leads to the formation of an acoustic wave. This phenomenon is also called photoacoustic effect [26]. When light is absorbed, some atoms become excited. They go from the ground state to a higher energy level. Upon returning to the ground state, heat energy is released [27]. According to the ideal gas law, an increase in temperature leads to an increase in pressure in a closed volume [26]. Subsequently, when the light source is turned off, the analyte cools and compresses, producing alternating pressures which create an acoustic wave [1]. The amplitude of the pressure signal is in relation to the gas concentration of the analyte [26]. The most commonly used device for detecting the acoustic wave is a microphone [27].
Depending on the desired level of accuracy and the specific range of measurement being

targeted, the design of a PAS is adaptable. The measurable range spans from a few parts per billion to 100% CO_2. The response time of the sensor is reliant on the gas flow and is thus restricted by turbulent effects resulting from excessive gas flow. [1]

1.3.3 Colorimetric Sensor

A colorimetric detector is a sensor based on the change of color of the pH indicator solution. An increase in CO_2 concentration leads to a decrease in pH value, resulting in a color change of a dye. The requirements for a dye are that it has a low air resistance and is stable. In addition to that no toxic fumes shall be produced [17]. This sensor principle has several advantages, including being inexpensive, straightforward, and unaffected by water vapor. Furthermore, there is potential for miniaturization. On the other hand, this approach has a slow response and recovery time. Nevertheless, colorimetric sensors have resolved these issues through modifications to the sensing material. So, it is also possible to use this sensor principle for breath-by-breath analysis [3].

1.3.4 Mass spectroscopy

Another technique for measuring CO_2 concentrations is mass spectrometry, which aims to separate gas according to its mass-to-charge ratio [18]. Mass spectrometry consists of three main components: an ionisation source, a mass analyser and a detector. The ion source ionises the neutral analyte and generates charged particles. These ions are then separated according to their mass-to-charge ratios using various principles, such as quadrupole and magnetic sector. The ion intensities are converted by the detector into an electrical signal [28]. Mass spectrometers are not widely used as they are bulky and quite expensive [18].

1.4 Thermal Conductivity Sensor

Another method of gas sensing is based on the physical principle of heat conduction [29]. The thermal properties of gases differ depending on the gas, which makes this principle useful for analysing analytes with thermal conductivities that differ significantly from the carrier gas, such as CO_2 and hydrogen (H_2) compared to nitrogen (N_2) [6]. This sensor principle has many applications, for example in gas chromatography [30]. Xenon detection during anesthesia is a common medical application [29].

1.4.1 Working principle

The thermal conductivity sensor is based on the transfer of heat caused by a temperature difference between a hot and a cold element. The amount of heat transfer depends on the thermal properties of the surrounding gases. Figure 9 shows a simplified depiction of

a thermal conductivity sensor. The heater is connected to a substrate and releases heat to the surroundings Q_A and the substrate Q_S. In this process, a portion of the heat is emitted to the substrate than to the surroundings. This reduces the temperature of the heater and therefore the amount of heat available for heat exchange with the environment. These losses can be minimised by using an appropriate heater geometry. [29]

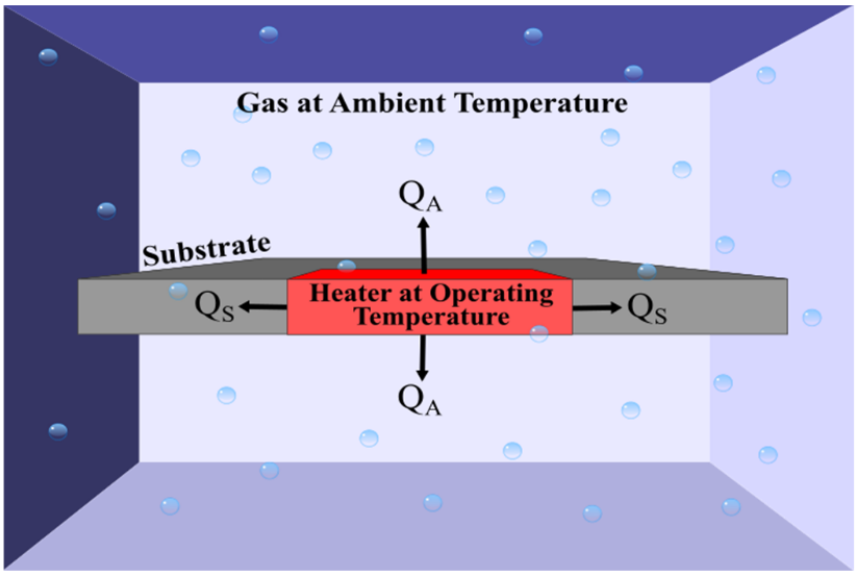

Figure 9: Simplified illustration of a thermal conductivity sensor. The heater releases heat to the connected substrate Q_S and to the surrounding medium Q_A. Source: [29]

Mahdavifar et al. [31] states the analytical description of the system using a lumped system analysis. Based on the energy balance principle, the amount of heat generated is equal to the amount of heat transferred. For the simplified model, this can also be written as

$$\dot{Q} = k_f A \left. \frac{dT_f}{dy} \right|_{wall} \tag{3}$$

where the amount of heat generated in the heater element is represented by $\dot{Q}$ and the thermal conductivity is represented by k_f. A is the surface area of the heater and $\left. \frac{dT_f}{dy} \right|_{wall}$ is the temperature gradient at the surface of the heater. The temperature gradient can be substituted by the heater temperature T, the ambient temperature T_∞ and the conduction length L, which is the distance between heater and the bulk. This leads to Formula 4:

$$\dot{Q} = k_f A \frac{(T - T_\infty)}{L} \tag{4}$$

where the rate of heat generation $\dot{Q}$, resulting from the application of an electrical bias, is equal to the consumed electric power I^2R. I stands for the electric current and R is the resistance. The resistance is temperature dependent, which is described by a linear model. By combining the linear model and substituting $\dot{Q}$ with the consumed electric

power, Formula 5 is obtained:

$$I^2 R_0 \left(1 + \alpha \left(T - T_\infty\right)\right) = k_f A \frac{(T - T_\infty)}{L} \tag{5}$$

This equation describes the working principle of a thermal conductivity sensor in steady-state operation [31]. Formula 5 shows that the temperature of the heater, and therefore its resistance, is related to the thermal conductivity of the surrounding medium. Thus, the heat and resistance of the heater will vary with the gas present in the medium [29]. By rewriting Formula 5, the temperature difference can be expressed by the heater geometry, the cold resistance, the temperature coefficient of the resistance and the thermal conductivity.

$$T - T_\infty = \frac{I^2 R_0 L}{k_f A - I^2 R_0 \alpha L} \tag{6}$$

As the resistance is temperature dependent, it can be described by the heater geometry, the cold resistance, the temperature coefficient and the thermal conductivity. Formula 7 shows the hot resistance R_2 in steady state.

$$R_2 = R_0 \left(1 + \alpha \frac{I^2 R_0 L}{k_f A - I^2 R_0 \alpha L}\right) \tag{7}$$

It is evident that gases with comparable thermal conductivities cannot be accurately detected. Due to this reason, this sensor principle has a disadvantage in terms of selectivity. The advantages of the sensor include low cost, low power, fast response time, long lifetime and a wide dynamic range [29].

1.4.2 Thermal properties of gases

Gases can be described in terms of different thermal properties. These include thermal conductivity, thermal diffusivity, specific heat and density [2]. Thermal conductivity describes how well a material conducts heat. Its unit is $\frac{\mathrm{W}}{\mathrm{mK}}$ [32]. Thermal conductivity values are within a wide range. Gases have a thermal conductivity of about 0.01 $\frac{\mathrm{W}}{\mathrm{mK}}$, whereas pure metals have a value of about 1000 $\frac{\mathrm{W}}{\mathrm{mK}}$ [33]. An overview of the thermal conductivity and other thermal properties of gases is given in Table 2. One of the properties listed in the table is the specific heat capacity in $\frac{\mathrm{J}}{\mathrm{kgK}}$. This parameter is the heat capacity, which is the amount of heat that can be stored by a material, normalised to its mass. Another thermal property of gases is the thermal diffusivity. Its unit is $\frac{\mathrm{m}^2}{\mathrm{s}}$. This parameter expresses how quickly heat is transferred through a material [32].

The thermal diffusivity and thermal conductivity are related according to Formula 8.

$$D = \frac{k_f}{\rho C_p} \tag{8}$$

D is the thermal diffusivity, k_f the thermal conductivity, ρ the density and C_p the specific heat capacity [34].

Table 2: Thermal properties of different gases at a temperature of 25°C and a ambient pressure of 1 Bar. Source: [2]

	Thermal Conductivity $\left[\frac{\text{mW}}{\text{mK}}\right]$	Specific Heat Capacity $\left[\frac{\text{kJ}}{\text{kgK}}\right]$	Thermal Diffusivity $\left[\frac{\text{mm}^2}{\text{s}}\right]$	Density $\left[\frac{\text{kg}}{\text{m}^3}\right]$
Air	26.2	1.01	22.3	1.17
N_2	25.9	1.05	22.0	1.17
CO_2	16.6	0.85	11.0	1.78
O_2	26.4	0.92	21.9	1.29
H_2	181	14.3	154	0.08
He	154	5.19	185	0.16
CH_4	34.0	2.22	23.6	0.65

Table 2 shows that the thermal conductivity of hydrogen is approximately seven times higher than that of the gases present in the atmosphere. The heat from the heating wire can be released more effectively into the enclosed gas mixture when the surrounding gas has a higher thermal conductivity. [35]

1.4.3 Measurement principles

For thermal conductivity sensors, steady-state and transient operations can be used as measurement methods. The working principle of the thermal conductivity sensor has already been explained using the steady-state method. Here, a DC current or voltage is applied to a wire to heat it up through Joule heating. During transient operation, a time-varying signal is applied to the heater. The hot wire method and the 3 omega method belong to this operation principle [29]. The following sections explain both methods.

Hot wire method

A voltage or current step is applied to a wire using the pulsed hot wire method. As a result of the Joule heating, the wire experiences an increase in temperature. This process depends on the thermal conductivity of the surrounding medium [29]. Formula 5 describes the thermal conductivity sensor in steady-state operation. To include the temperature change from the ambient temperature T_∞ to the hot temperature resulting from the applied voltage step, the equation is modified by adding a transient term

$$I^2 R_0 \left(1 + \alpha \left(T - T_\infty\right)\right) = \rho V C_p \frac{dT}{dt} + k_f A \frac{(T - T_\infty)}{L} \tag{9}$$

where ρ is the density of the system [31]. C_p is the specific heat capacity and overall the term $\rho\, C_p V$ represents the thermal mass [29].

According to Gardner et al. [29] the time resolved solution of Formula 9 can be obtained and further transformed to determine the time constant τ:

$$T - T_\infty = \frac{I^2 R_0 L}{k_f A - \alpha I^2 R_0 L} \left(1 - e^{-\frac{t}{\tau}}\right) \tag{10}$$

$$\tau = \frac{C_p L \rho V}{k_f A - \alpha I^2 R_0 L} \tag{11}$$

The equations demonstrate that the time constant is inversely proportional to the thermal conductivity. Additionally, the temperature change follows an exponential pattern. Since the resistance is temperature dependent, it is expected that the resistance change will also be exponential [29]. Mahdavifar et al. [31] described the alteration in resistance resulting from a change in temperature can be quantified using the Formula 12:

$$R = R_2 + (R_0 - R_2) e^{-\frac{t}{\tau}} \tag{12}$$

R_2 is the hot resistance in steady state, which has already been described by Formula 7. Figure 10 shows the exponential resistance curve in response to a voltage step.

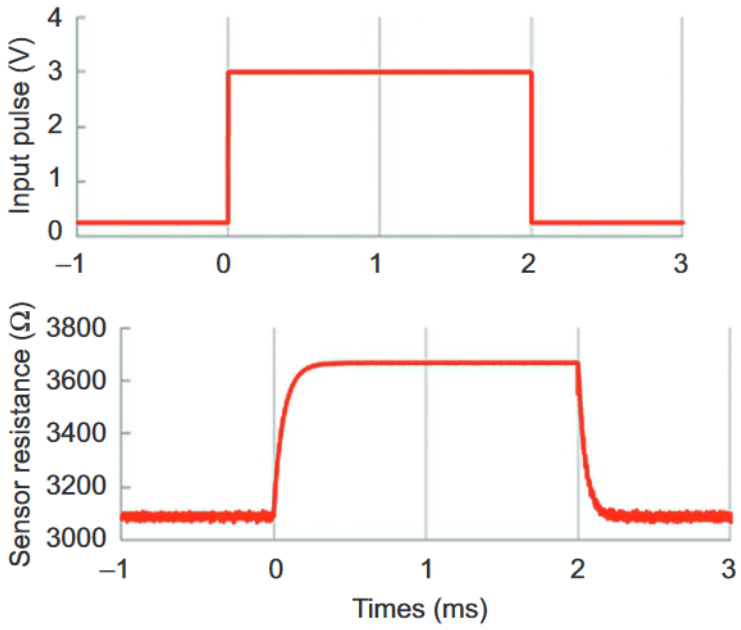

Figure 10: The input voltage pulse and the sensor resistance over time. The resistance increases exponentially to its maximum. The time constant and the maximum value of the resistance is depending on the thermal conductivity of the surrounding medium and on the input power. Source: [31]

In addition to the time constant, the height of the resistance change is also an important quantity for evaluation [6]. For example, a low thermal conductivity causes a high change in resistance [35]. The time constant and resistance increase as the input power I^2R increases, allowing for better sensor sensitivity [31]. Advantages of this measurement technique is that the measurement time is very short and the power consumption is low [29].

3 omega method

Another measurement principle used in transient operation is the 3 omega method [29]. In contrast to the hot wire method, the 3 omega method offers better sensitivity and resolution [6].

According to Gardner et al. [29] the heater is supplied with a sinusoidal current at a frequency of ω.

$$I(t) = I_\omega \, cos(\omega t) \tag{13}$$

Due to Joule heating, power P is dissipated.

$$P = I^2 R \tag{14}$$

By inserting Formula 13 into Formula 14, Formula 15 is obtained:

$$P(t) = 0.5 {I_\omega}^2 \, R_0 \, (1 + cos(2\omega t)) \tag{15}$$

R_0 is the resistance of the heater at 25°C [29].
The power causes a temperature change ΔT of the heater and remaining derivation of the output voltage is explained by Kühnel et al. [36]:

$$\Delta T(t) = \Delta T_{2\omega}\, cos(2\omega t + \varphi) \tag{16}$$

$\Delta T_{2\omega}$ is the amplitude of the temperature change. This parameter provides information about the thermal conductivity. The phase shift caused by the inertia of the Joule heating is represented by φ. As the resistance is dependent on temperature, it also varies with changes in temperature:

$$R(t) = R_0(1 + \alpha \Delta T_{2\omega}\, cos(2\omega t + \varphi)) \tag{17}$$

α is the linear temperature coefficient of the resistance. Inserting Formulae 13 and 17 into Ohm's Law U = RI yields Formula 18:

$$U(t) = R_0 I_0 cos(\omega t) + \frac{R_0 I_0\, \alpha\, \Delta T_{2\omega}}{2} cos(\omega t + \varphi) + \frac{R_0 I_0\, \alpha\, \Delta T_{2\omega}}{2} cos(3\omega t + \varphi) \tag{18}$$

$$U(t) = U_0\, cos(\omega t) + \frac{U_0\, \alpha\, \Delta T_{2\omega}}{2} cos(\omega t + \varphi) + \frac{U_0\, \alpha\, \Delta T_{2\omega}}{2} cos(3\omega t + \varphi) \tag{19}$$

The voltage component at 3ω can be measured directly with a lock-in amplifier. Considering only the third harmonic voltage, Formula 19 can be rewritten.

$$U_{3\omega,rms} = \frac{U_0\, \alpha\, \Delta T_{2\omega}}{2} \tag{20}$$

This formula describes the voltage of the third harmonic change only with respect to the temperature [36]. The relation between the signals is visualized in Figure 11.

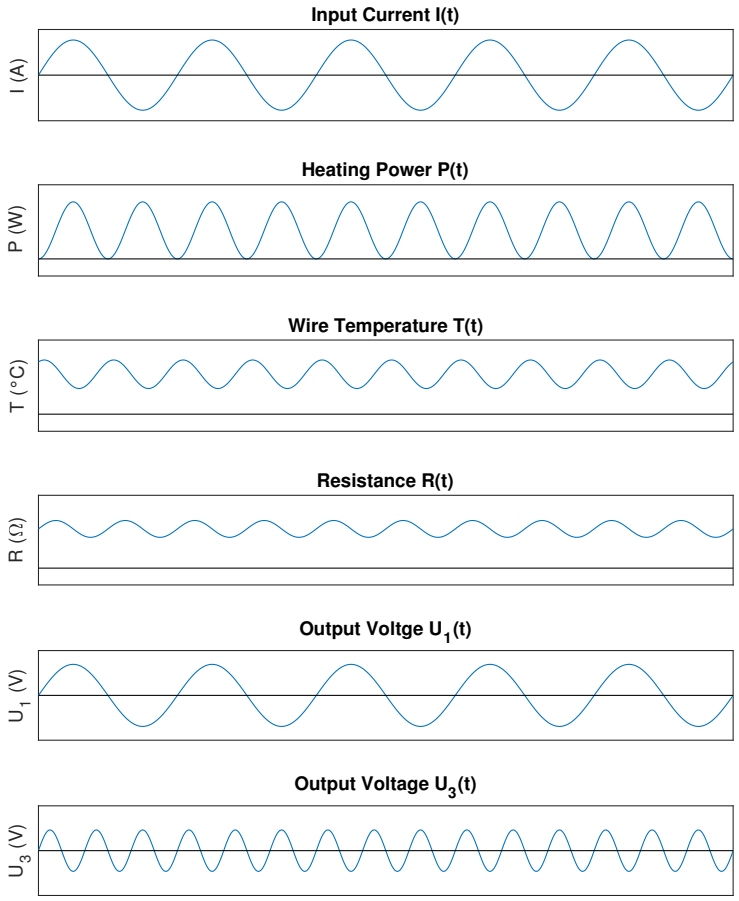

Figure 11: Input current I, heating power P, temperature T, resistance R and output voltage U. The input current which is applied to the heater has the frequency ω. The resulting heating power has the frequency 2ω. Due to Joule heating the temperature has a frequency of 2ω and a phase shift φ. As the resistance is temperature dependent, it is in phase with the temperature signal. The output voltage has frequency components at ω and 3ω. Source: Adapted from [29]

The measurement setup used for this method consists of the sensor, a power supply, a source meter and a lock-in amplifier [6]. The lock-in amplifier has the task of extracting the amplitude and the phase shift of the resulting signal [29]. However, this device limits the temporal response of the sensor system [30]. Another drawback of the 3 omega method is the complicated electronics and post-processing that are required [29].
With the measurement setup, four quantities that are of interest for the evaluation are determined: the amplitude of the 3 omega signal, the in-phase and out-of-phase components of the signal, and the phase [6].
The 3 omega signal depends not only on the gas concentration of the surrounding but also on the amplitude and frequency of the input current. At low frequencies the system is quasi-static. The main influence on the 3 omega signal in this frequency range is thermal conductivity. The thermal transient characteristics of the sensor have almost no effect on

the output voltage. The lower the thermal conductivity of the surrounding medium, the greater the temperature oscillations. There is also no phase lag at low frequencies. This frequency range is suitable for measuring mixtures by their thermal conductivities.
At high frequencies, there are almost no temperature oscillations due to the limited penetration depth of the thermal wave.
At intermediate frequencies the output phase lag is mainly influenced by the thermal transient properties of the gas and the sensor [30]. The dominant property in this context is the thermal diffusivity, D, which describes the speed of heat transfer [6].
By using both thermal conductivity and thermal diffusivity, it is possible to improve the distinction between gases. Table 2 shows that the thermal conductivity of CO_2 is about 37% different from that of air, and for thermal diffusivity, the difference is about 51% [2].

1.4.4 Cross Sensitivities

Parasitic factors can affect the output signal of a thermal conductivity sensor. These inferences include temperature, humidity, pressure, and gas turbulence [6]. The subsequent sections provide a concise overview of these unwanted effects.

Temperature
The thermal conductivity of materials is affected by temperature, regardless of the measurement method used. Formula 5 demonstrates how the sensor output is affected by the ambient temperature during steady-state operation. The impact of temperature on the output signal can also be observed in Formula 10 for the hot wire method and Formula 19 for the 3 omega method [29]. As can be seen from Figure 12, thermal conductivity rises as the temperature rises [33]. The Figure illustrates that the thermal conductivity increases to different extents with rising temperature, depending on the gas [29].
The relationship between thermal conductivity and temperature can be represented by a fourth order term:

$$k_f = A + BT + CT^2 + DT^3 + ET^4 \tag{21}$$

The values of the coefficients A to E in the equation above, which are substance-dependent, can be found in the VDI Heat Atlas [35].

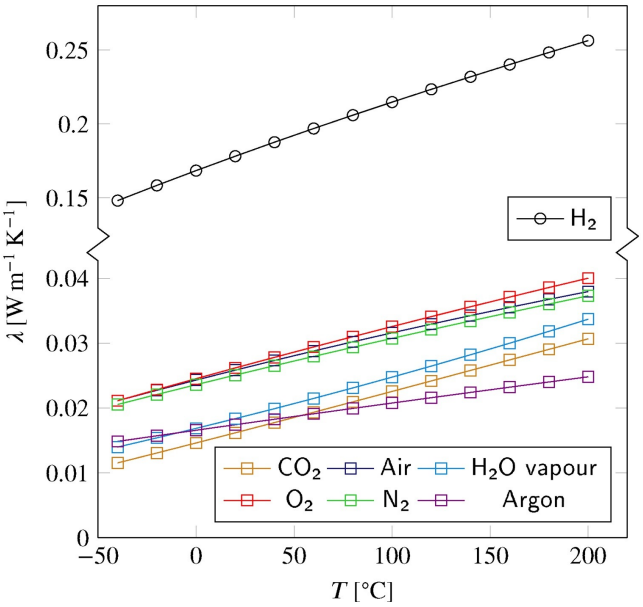

Figure 12: Thermal conductivities of different gases at different temperatures. As the temperature rises, the thermal conductivity increases at different rates depending on the gas. Source: [35]

Compensation is necessary as temperature can have a dominant effect on the output signal, rather than thermal conductivity. A common compensation method involves using a separate temperature sensor to compensate for temperature during post-processing. [29]

Humidity

Changes in humidity can affect thermal conductivity, making it a parasitic effect. Furthermore, a correlation exists between temperature and humidity, as higher temperatures enable the air to hold more water vapour. Therefore, for the same relative humidity, the effect on thermal conductivity is much greater at high temperatures. Figure 13 illustrates this relationship between thermal conductivity, temperature, and humidity. The effects of humidity on compensation have not been thoroughly researched yet. One method is to include an extra humidity sensor and compensate for the effect with a post-processing algorithm. [29]

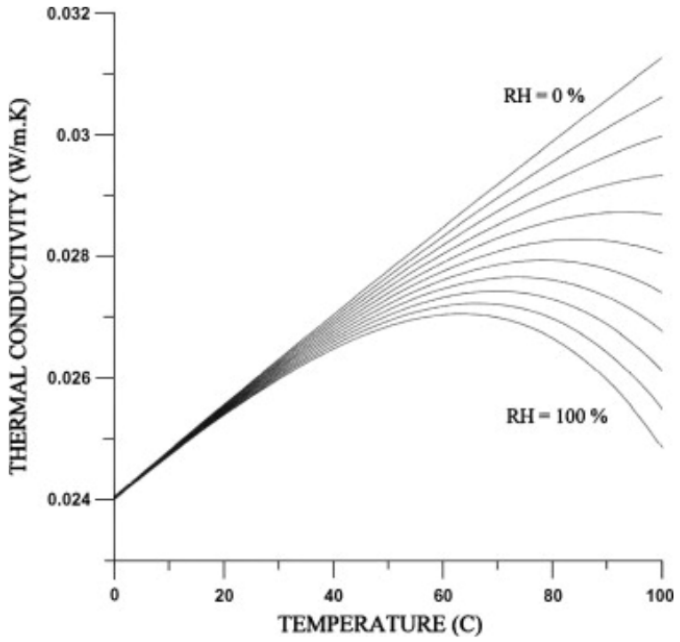

Figure 13: Thermal conductivities of air for different temperatures and relative humidities. Source: [29]

Pressure

The sensor output is also affected by pressure. Although pressure has a relatively small impact on the sensor output compared to temperature and humidity, it still needs to be taken into account and compensated for [35]. The effect of pressure varies depending on the pressure range, as illustrated in Figure 14.

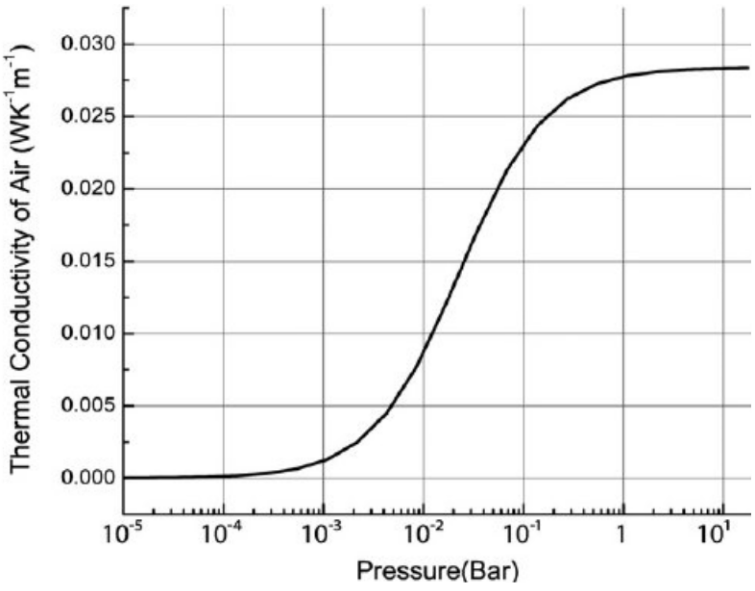

Figure 14: Thermal conductivity of air at different pressures. Between 10^{-3} bar and 10^{-1} bar the thermal conductivity changes significantly with the pressure. Above 1 bar there is only a minor effect on the thermal conductivity. Source: [29]

At pressures above 1 bar, there is only a minor effect on thermal conductivity. In the pressure range of 10^{-3} bar to 10^{-1} bar, thermal conductivity varies significantly with pressure. In addition to affecting thermal conductivity, pressure can also induce mechanical stress on the sensor structure. For pressure compensation is commonly an addition pressure sensor used and an algorithmic compensation. [29]

2 Methods

The following section outlines the methods and materials used. After a brief concept phase, the 3 omega method was first simulated and then tested using the available hardware. Next, an overview of the setups used is provided, followed by the conducted characterisations. This includes the definition of the CO_2 sensitivity, as well as humidity and temperature characterisation. This information was used to implement a compensation algorithm. Finally, the application was tested.

2.1 Concept Considerations

Prior to implementation, it was important to establish the necessary requirements to ensure accurate measurement of CO_2 in exhaled breath. The measurement range and accuracy required are stated in the standard ISO 21647:2004 [23]. The required measurement range is between $0 - 10\,\%$, or in mmHg, between 0 and 76 mmHg. The measurement accuracy of CO_2 is defined in Formula 1 and visualized in Figure 15.

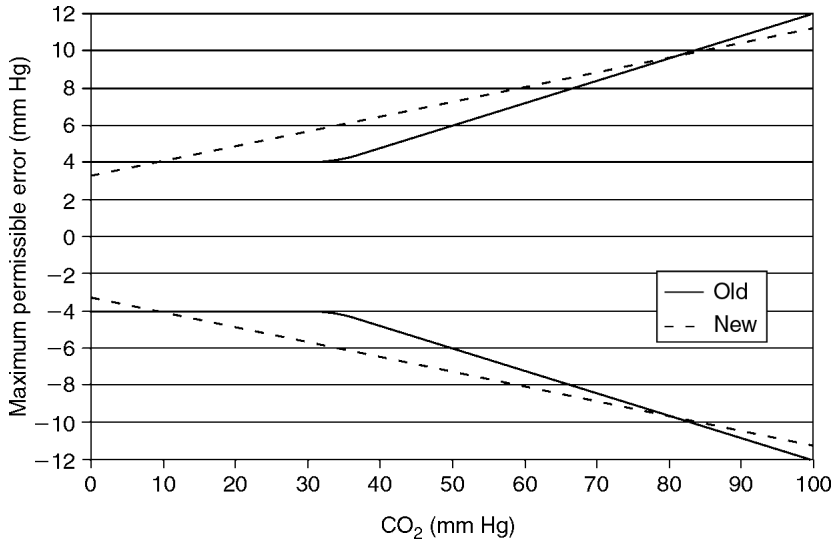

Figure 15: The discrepancy between the maximum permissible error in mmHg of the former standard (ISO 9918, 1993) and the current standard (ISO 21647, 2004). Source: [23]

This figure illustrates the discrepancy between the maximum permissible error in mmHg of the former standard (ISO 9918, 1993) and the current standard (ISO 21647, 2004). For the current standard, the maximum permissible error in the measurement range between 35-40 mmHg is approximately ± 6 mmHg. Upon recalculation of the maximum permissible error in percentage terms, a value of $\pm 0.79\,\%$ is obtained at atmospheric pressure.
During the concept phase, the technical specifications of existing capnography equipment were taken into account. Here, the datasheets of CO_2-Modul DG 2002 C [38] and capONE Nihon Kohden [39] were utilised. Both devices have the same measurement range as the standard states. The datasheets define the measurement accuracy as 10% of the reading.

Considering both the standard and this information, the desired accuracy was set as 0.5%. Kliche et al. [2] further note that 0.5% is accurate enough for determining whether a lung is healthy or not.
Another factor to consider was the sampling time. The desired sampling time was set to 10 ms, allowing for the dynamic CO_2 curve to be obtained without any loss of information. In the following there is an overview of the discussed and set technical specifications:

- Measurement range: $0 - 10\%$
- Measurement accuracy: 0.5%
- Sampling time: 10 ms

The expected value for CO_2 sensitivity is approximately 60 $\mu V/\%CO_2$. This expectation is on the basis of measurements which have already been carried out with hydrogen. The known sensitivity to hydrogen of the used sensor is about 500 $\mu V/\%H_2$. As the thermal conductivity of H_2 is about 8 times higher than of CO_2, the expected sensitivity to CO_2 is one eighth of the known H_2 sensitivity.

2.2 CO_2 Sensor

The CO_2 sensor used for the measurements is a thermal conductivity (TC) sensor from Infineon Technologies AG. The sensor configuration comprises a resistive full bridge with sensor (s) and reference (r) elements, as illustrated in Figure 16. The pin configuration of the sensor is also shown in this figure. The sensor bridge output signals are measured at pin 8 (VB-) and pin 9 (VB+). The supply voltage of pin 13 (EPI) should be equal to or greater than the supply voltage of the sensor to ensure correct operation.

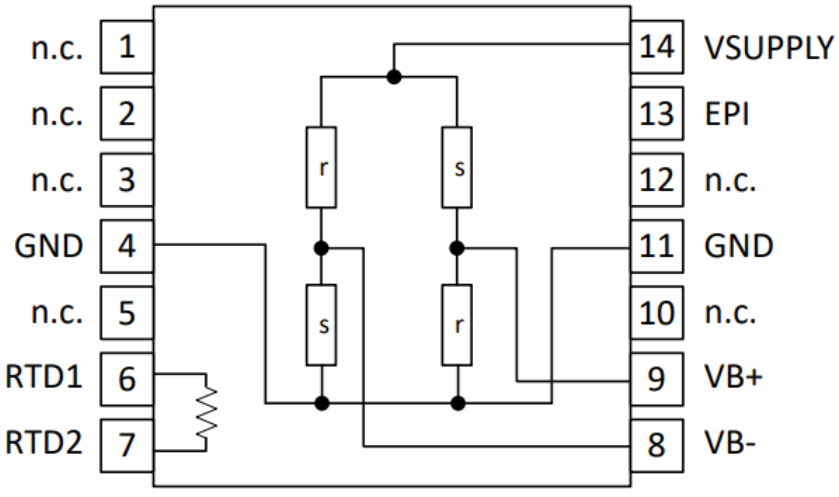

Figure 16: Pin layout of the TC CO_2 sensor

The CO_2 sensor was initially characterised using the hot wire method. To achieve this, a 5 V voltage pulse with a length of 100 ms was applied to the sample using a single measurement unit (SMU). As SMU a National Instruments PXIe-4139 connected to a National Instruments PXIe-1088 was used. The transient response of the sensor was displayed using InstrumentStudio, a software developed by National Instruments for data collection and analysis. The thermal time constant was then determined by using the two cursors of the software.
Another value to be determined is the resistance of the sensor. A Keithley 2400 SMU was used to perform this task.

2.3 3 Omega Measurements

Prior to applying the 3 omega method to the CO_2 sensor in bridge configuration, the measurement method was first applied to a single wire sample. A current source was used to apply a sinusoidal signal to the sensing resistance. The voltage was measured using an oscilloscope. The resulting data was transferred to a PC via a USB cable for evaluation in MATLAB R2020b (MathWork Inc., Natick, Massachusetts, USA). Figure 17 illustrates the setup.

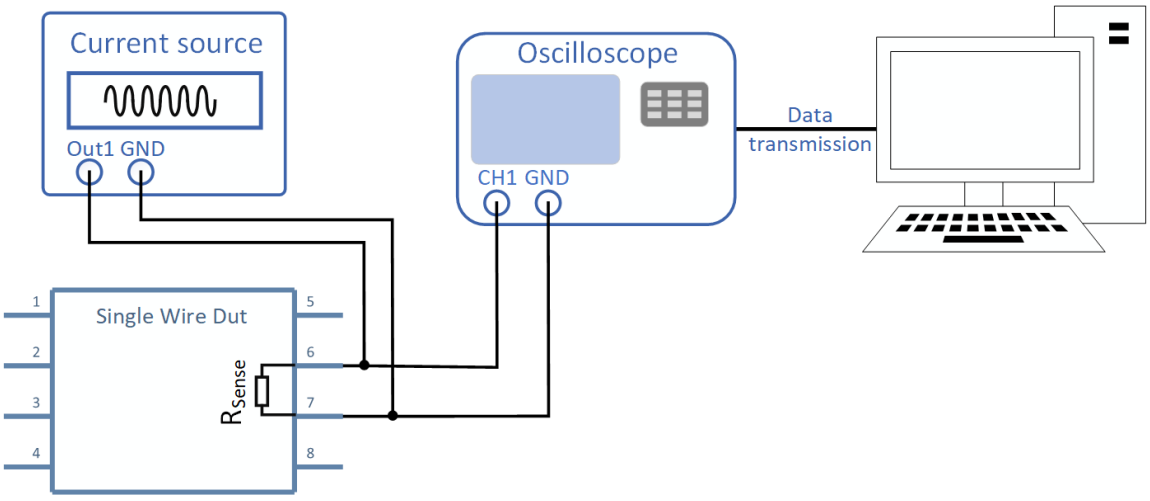

Figure 17: Setup for the measurements with the 3 omega method. The setup consists of a current source, the CO_2 sensor in single wire configuration, an oscilloscope and a computer to read in the oscilloscope data

Measurement procedure

The applied current had an amplitude of 2 mA. The offset was set to 0 A. The frequency was set to 5, 10, 30, 100, 500 and 1000 Hz. VISA USB was used to transfer the oscilloscope data to the computer. The read-out algorithm for the oscilloscope data was implemented in MATLAB R2020b. The measurement was performed while the sample was exposed to air and then to 2.5% H_2 in 97.5% N_2.

Overview of the set values:

- $I_p = 2\,mA$
- $I_{Offset} = 0\,mA$
- f = 5, 10, 30, 100, 500 and 1000 Hz

As it was not possible to measure the temperature oscillations with the used setup, the following equation, stated by Berndt et al. [6], can be used to determine ΔT for the voltage $V_{3\omega}$:

$$\Delta T = \frac{2V_{3\omega}}{\alpha R I} \tag{22}$$

α is the temperature coefficient of the heating wire, R is the resistance of the sensor at room temperature and I is the root-mean-square (RMS) value of the applied current.

Hardware components
The hardware components of this setup are:

- Current source: Keithley 6221 Current Source
- CO_2 Sensor: Single Wire TC sensor
- Oscilloscope: Teledyne Lecroy HD06104
- 2.5% H_2 in 97.5% N_2

Software components
The used software is listed in the following:

- MATLAB R2020b (MathWork Inc. , Natick, Massachusetts, USA):

  Read in oscilloscope data

  Data evaluation of measurements

2.4 3 Omega Simulation

To validate the measured results, a simulation of the 3 omega method on a single wire was performed using Simulink 2022b. A frequency sweep was performed to examine the frequency response of the system. The simulation was repeated for the thermal conductivity of air, 2.5% H_2 in N_2 and 100% CO_2.
During post processing, the measured signal, which represents the temperature of the wire T_{wire}, was Fourier transformed. By extracting the third harmonic of the transformed signal, the amplitude of the desired temperature signal was obtained. The resulting amplitudes were plotted against the corresponding frequencies.

The utilized model consists of a current source that supplies a temperature dependent resistor. The voltage and current are then measured across the resistor to determine the consumed power, which is equivalent to the generated heat and affects the resulting temperature of the wire. The heating of the wire is modelled as low-pass behaviour. The simulation schematics are depicted in Figure 18.

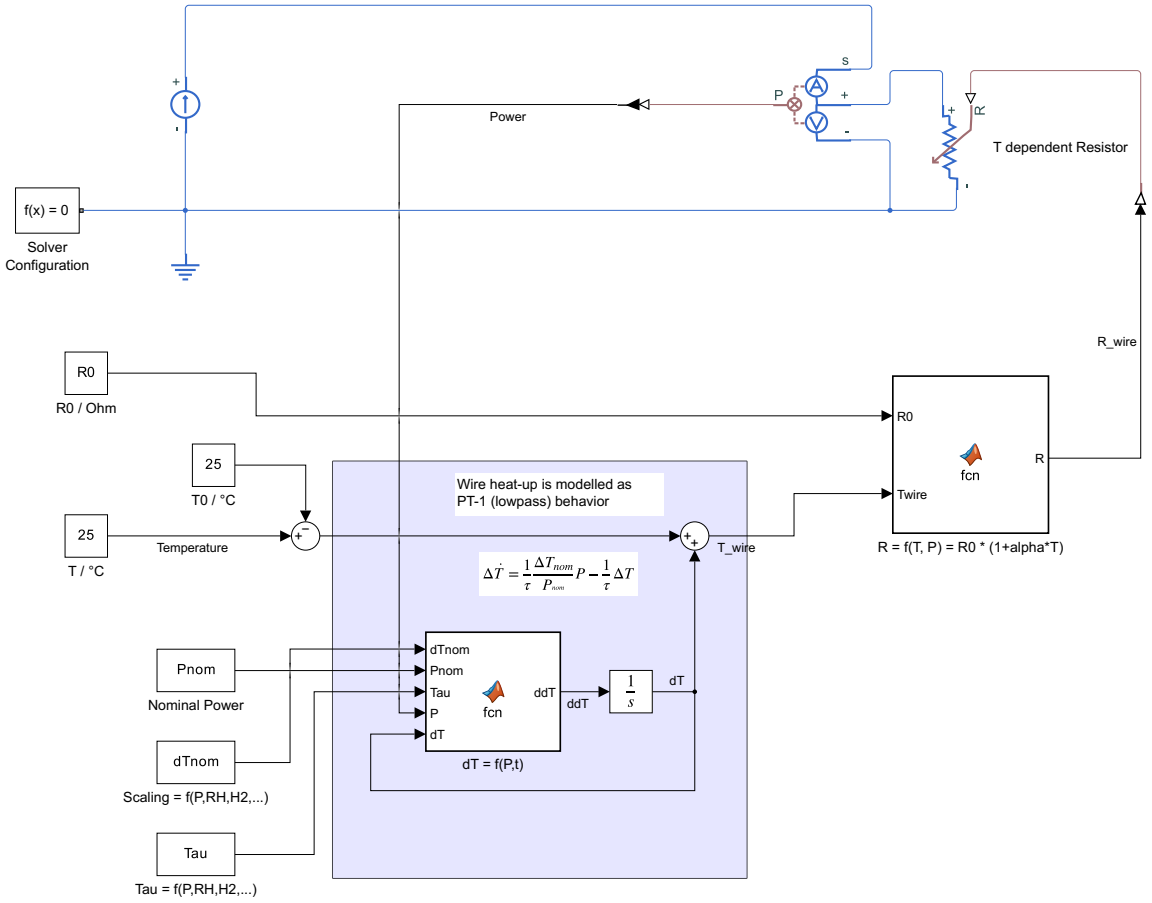

Figure 18: The simulation includes a current source, a temperature dependent resistor and a low-pass behaviour describing the temperature change of the wire.

The resistor is modelled with a linear temperature dependence, as shown in Formula 23:

$$R = R_0(1 + \alpha T_{Wire}) \tag{23}$$

α is the temperature coefficient and is equal to 0.0014 $\frac{1}{\mathrm{K}}$.
The wire heating model is represented by a first order low pass filter based on Formula 9. The measured power P at the resistor is substituted for the left side of the equation, treating temperature and resistance as separate systems. The resulting differential equation is presented in Formula 24:

$$P = \rho V C_p \Delta\dot{T} + k_f A \frac{\Delta T}{L} \tag{24}$$

By rearranging of the Formula 24, Formula 25 can be obtained:

$$\Delta\dot{T} = \frac{1}{\rho V C_p} P - \frac{k_f A}{L \rho V C_p} \Delta T \tag{25}$$

The coefficient preceding ΔT is equivalent to the inverse of the thermal time constant τ.

$$\tau = \frac{L \rho V C_p}{k_f A} \tag{26}$$

Compared to the thermal time constant stated in Formula 11, the term $\mathrm{I^2R_0L}\alpha$ in the denominator is missing. This introduces an inaccuracy in the simulation. The ratio between $\mathrm{k_f A}$ and $\mathrm{I^2R_0L}\alpha$ is dependent on the thermal conductivity, but remains within the range of 0.1.
As the temperature change also affects the power P, τ is added to scale it.

$$\Delta\dot{T} = \frac{1}{\tau} \frac{L \rho V C_p}{k_f A} \frac{1}{\rho V C_p} P - \frac{1}{\tau} \Delta T \tag{27}$$

$$\Delta\dot{T} = \frac{1}{\tau} \frac{L}{k_f A} P - \frac{1}{\tau} \Delta T \tag{28}$$

At steady state, $\Delta\dot{\mathrm{T}}$ is equal to zero and both the power and temperature reach their nominal values, $\Delta\mathrm{T_{nom}}$ and $\mathrm{P_{nom}}$. The nominal power is shown in Formula 29:

$$P_{nom} = k_f A \frac{\Delta T_{nom}}{L} \tag{29}$$

Formula 29 can be modified by including ΔT_{nom}. This allows for the insertion of P_{nom}.

$$\Delta\dot{T} = \frac{1}{\tau}\frac{L}{k_f A}\frac{\Delta T_{nom}}{\Delta T_{nom}}P - \frac{1}{\tau}\Delta T \tag{30}$$

$$\Delta\dot{T} = \frac{1}{\tau}\frac{\Delta T_{nom}}{P_{nom}}P - \frac{1}{\tau}\Delta T \tag{31}$$

In steady state, this equation fulfils the requirement of being zero.

$$\Delta\dot{T} = \frac{1}{\tau}\frac{\Delta T_{nom}}{P_{nom}}P_{nom} - \frac{1}{\tau}\Delta T_{nom} \stackrel{!}{=} 0 \tag{32}$$

For the values τ, ΔT_{nom}, and P_{nom} measured values were used. These were obtained from the gas-sensor-system. They were influenced not only by the thermal properties of the gas but also by the sensor and its geometry.
The nominal temperature ΔT_{nom} was determined by measuring the temperature change of the sensing wire in steady state when a voltage of 5.5 V was applied. The nominal power P_{nom} was calculated by using the measured resistance change at 5.5 V and the applied voltage.
ΔT_{nom} was scaled according to the thermal conductivity set in the simulation.
τ was assumed to be constant. Formula 26 demonstrates that the value is dependent on thermal conductivity, meaning that it will change if a different thermal conductivity is used in the simulation. This was not considered in this simulation. However, this did not affect the steady state temperature value.
In addition this simulation only represents the temperature dependent resistance. The total resistance of the sample consists of a constant resistance and a temperature dependent resistance. The constant resistance is not considered.
It should be noted that the model is based on a simplified Formula. This Formula is based on a lumped system analysis. It is also assumed that there are no heat losses and that the heat transfer is in one direction only.

Software component
The software used for this simulation:

- SIMULINK 2022b (MathWork Inc. , Natick, Massachusetts, USA)

2.5 Used Setups

After initial investigations into the 3 omega method, it was decided to proceed with the hot wire method in steady state to meet the previously established requirements. The hot wire measurement can be performed using either the DevKit setup or the Single Dut setup. Further details on both setups are provided below.

2.5.1 DevKit

For initial measurements, an already available set up was used. The DevKit comprises a motherboard, a daughterboard, and a graphical user interface (GUI). The power supply provides the setup with a 12 V voltage. The motherboard contains a microcontroller that regulates the supply voltage of the CO_2 sensor, processes data, and transmits it. The daughterboard contains both a TC CO_2 sensor and a humidity sensor. The GUI displays the data that has been transmitted to the computer. Additionally, the voltage settings for the CO_2 sensor can be adjusted. Figure 19 illustrates a bloc diagram of the setup.

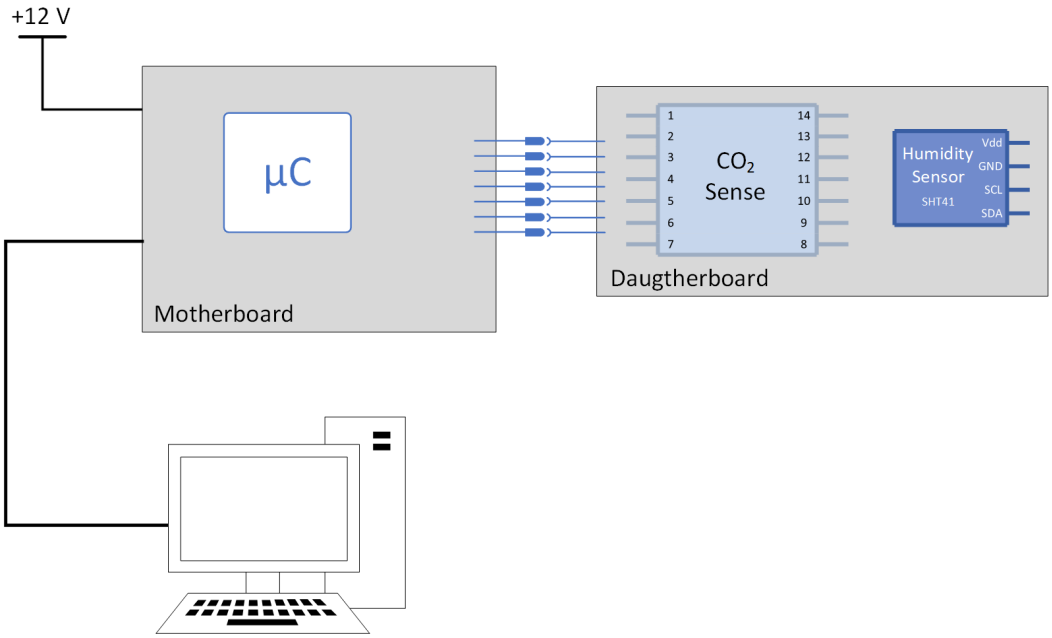

Figure 19: DevKit setup. The main component of the motherboard is a microcontroller that regulates the supply voltage of CO_2 sensor, processes data and transmits it. The daughterboard contains the TC CO_2 sensor and a humidity sensor. The power supply provides 12 V.

Measurement procedure
The GUI enables the adjustment of the amplitude, pulse width, and period of the supply voltage for the CO_2 sensor. A voltage of 5 V was used for the amplitude. The period of the pulse signal was 100 ms, and the pulse width was 10 ms. The minimum sampling time for this setup was 100 ms. The data was saved as a .txt file and evaluated in Matlab R2020b.

Hardware component

- DevKit

Software components
The software used are listed below:

- GUI

  Setting supply voltage for CO_2 sensor

  Read in data

- MATLAB R2020b (MathWork Inc. , Natick, Massachusetts, USA):

  Data evaluation

2.5.2 Single Dut Setup

As the DevKit is not suitable for all measurements, another setup is required. The DevKit is not suitable for pressure chamber measurements and the sampling time is limited to 100 ms, which does not meet the required 10 ms.
The Single Dut setup comprises a printed circuit board (PCB) that contains the CO_2 sensor, a humidity sensor and a pressure sensor. The humidity sensor can be chosen between two sensors from Sensirion: SHT21 and SHT41. In addition to humidity, the SHT21 and SHT41 sensors are also capable of measuring temperature. The pressure sensor used is the TE Connectivity MS5803-14BA. One of the outputs of the triple supply powers the two sensors, while the remaining two outputs power the PCB. The data collected by the humidity and pressure sensors is transmitted using Inter-Integrated Circuit (I2C) communication.
The CO_2 sensor was supplied with a voltage pulse. The output signals of the CO_2 sensor at pins 8 and 9 were amplified by an amplifier and converted to a digital signal using an analog-to-digital converter (ADC) which was configured using Keil μVision 5.0. The amplifier and the ADC together is called Measurement Interface (MEIF). The data was transmitted via Universal Asynchronous Receiver Transmitter (UART) and read in H-Term. The humidity, temperature, pressure and CO_2 data were evaluated in MATLAB R2020b. An overview of the setup is visualised as a block diagram in Figure 20.

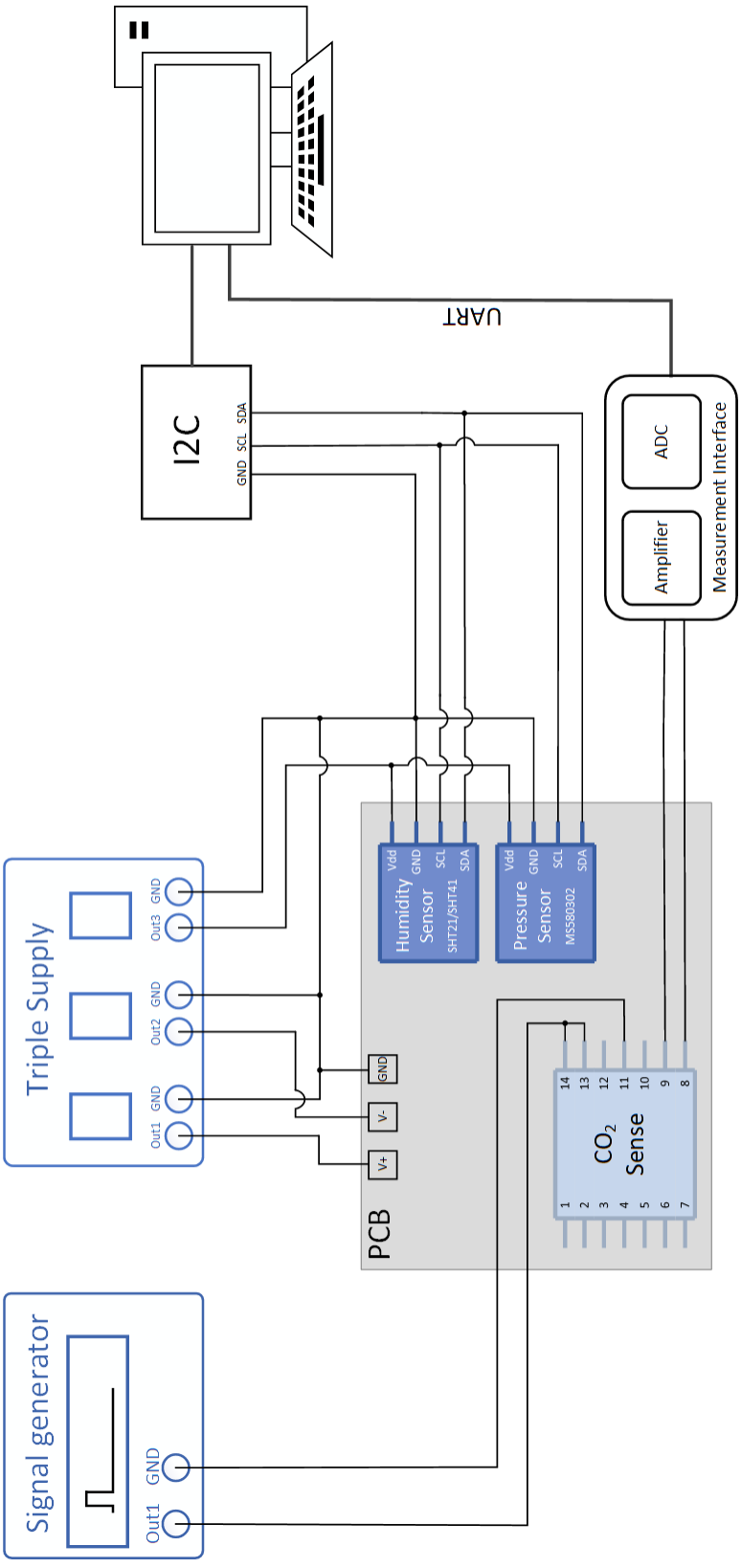

Figure 20: Single Dut setup. The PCB contains the CO_2 sensor and two additional sensors for humidity, temperature and pressure measurement. The data of the CO_2 sensor is transmitted via UART communication.

Hardware components

- TE Connectivity MS5803-14BA

  Pressure sensor with I2C bus interface [40]

- Sensirion SHT21

  Humidity and temperature sensor with I2C interface

  Response time humidity (τ 63%): 8 s

  Operating range humidity: 0 - 100% rH

  Response time temperature (τ 63%): 5 to 30 s [41]

- Sensirion SHT41

  Humidity and temperature sensor with I2C interface

  Response time humidity (τ 63%): 4 s

  Operating range humidity: 0 - 100% rH

  Response time temperature (τ 63%): 2 s [42]

- CO_2 TC sensor
- Triple Supply: Keysight E36313A
- Signal generator: Keysight 33220A
- I2C: National Instruments USB-8452

Software components

- Keil μVision 5.0 (Arm Germany GmbH)

  Software tool for the development of embedded systems

- HTerm 0.8.9 (Tobias Hammer):

  Terminal program for serial communication

- MATLAB R2020b (MathWork Inc. , Natick, Massachusetts, USA)

  Data evaluation

2.6 Sensitivity Determination

The CO_2 sensitivity of the TC CO_2 sensor was determined by integrating the DevKit into an existing gas setup. The setup comprised two gas bottles, a pressure chamber, and software-controlled flow meters. One gas cylinder contained synthetic air with 2% CO_2, while the other was filled with synthetic air. The gas concentrations in the pressure chamber were set using flow meters.

For sensitivity determination, the CO_2 concentration was set to 500, 1500, 3000, and 6000 ppm CO_2. The GMP343 sensor was used as a reference to verify the accuracy of the set concentration. In addition to the TC CO_2 sensor, a photoacoustic sensor was also used to measure the CO_2 concentration. In order to determine the sensitivity, the `fit` function from MATLAB R2020b was employed during the data evaluation process. This function fits a linear polynomial curve to the acquired CO_2 concentration, as measured by the GMP343, and the output voltage, as measured by the TC Sensor.

Humidity, temperature and pressure sensors were also placed in the pressure chamber. The Sensirion SHT41 was used for humidity and temperature measurement, while a differential pressure sensor was used for pressure sensing. This setup is visualised in Figure 21. The obtained data was transmitted via cable ducts from the pressure chamber to the computer. The evaluation of the data was performed using MATLAB R2020b.

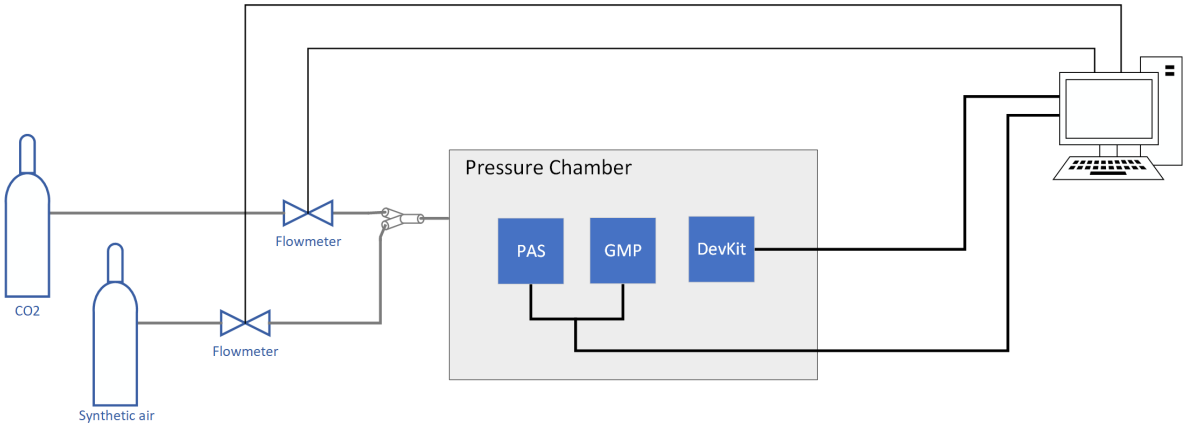

Figure 21: Setup for determining CO_2 sensitivity. The pressure chamber contains three CO_2 sensors, two of which are used as references. The steps for CO_2 are set by software controlled flow meters.

Hardware components

- Gas cylinder 2% CO_2, 98% synthetic air
- Gas cylinder 100% synthetic air
- Pressure chamber

- Software-controlled flow meters
- Reference sensor: Vaisala GMP343
- DevKit
- CO_2 TC sensor
- PAS CO_2 sensor from Infineon Technologies AG

Software components

- DevKit GUI: setting supply voltage for CO_2 sensor
- Software to set CO_2 concentrations
- MATLAB R2020b (MathWork Inc., Natick, Massachusetts, USA): data evaluation

2.7 Humidity Characterisation

To characterise the humidity of the sample, a bubbler was integrated into the Single Dut Setup. The bubbler consisted of a glass bottle half filled with water. Dry air was passed through a pneumatic tube from the compressor to the inlet port of the glass bottle. The air was then humidified by passing through a glass tube immersed in water contained in the bottle. The humidified air was then directed through another pneumatic tube from the outlet of the bottle to a solenoid valve. Upon opening the solenoid valve, a humidity step was generated. The humid air was then passed through a tube into a pressure chamber, where the humidity and CO_2 sensors were located. Before the solenoid valve opened, the pressure chamber was flushed with dry air. The setup is visualised as bloc diagram in Figure 22.

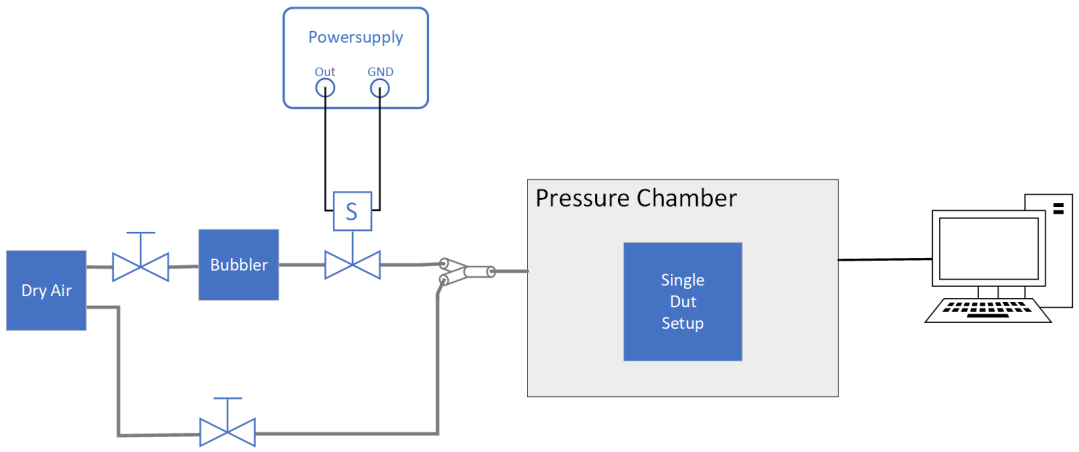

Figure 22: Setup for humidity characterisation. The setup consists of the single dut setup within a pressure chamber. Addtionally a bubbler was added to the setup to produce humidified air.

Measurement procedure

At first the pressure chamber was flushed with dry air. The measurement started when a voltage was applied to the CO_2 sensor. The sampling time was set to 50 ms to enable proper measurement of the step response of the sensor. Altogether, 200 points were measured. The initial 20 measurement points were taken when the pressure chamber was dry. After 20 measurement points, the valve opened, and humid air entered the pressure chamber. The measurement was repeated 15 times. The humidity was measured by using the SHT21. The data obtained from the CO_2 and humidity sensors were analysed using MATLAB R2020b. The sensitivity to humidity was determined by fitting a linear polynomial curve on the measured humidity of the dry and humid air and on the voltage of the TC sensor at the dry and humid states.

Hardware components

- Single Dut Setup
- Bubbler
- Manual valves
- Solenoid valve: Festo MHJ10-S-2,5-QS-6-HF

Software components

- Keil μVision 5.0 (Arm Germany GmbH)
- MATLAB R2020b (MathWork Inc., Natick, Massachusetts, USA): data evaluation

2.8 Temperature Characterisation

To determine the temperature dependency of the sensors, a thermostream was used. The head of the thermostream was placed over the TC CO_2 sensor, the humidity sensor and the pressure sensor. A temperature sweep was then conducted. During the measurement, the humidity was kept constant because it also affects the measured output. Several measurement points were taken for each temperature step to ensure temperature stabilization. The data was evaluated in MATLAB R2020b to determine its sensitivity to temperature.

Hardware components

- Single Dut Setup
- Thermostream

Software components

- MATLAB R2020b (MathWork Inc., Natick, Massachusetts, USA): data evaluation

2.9 Compensation Algorithm

As previously stated, a TC sensor also responds to variations in temperature, humidity, and pressure. To obtain a CO_2 curve without the influence of any cross sensitivities, it was necessary to compensate for these parasitic effects during post processing. Additional sensors were used to measure these parameters. Due to equipment limitations, several assumptions had to be considered. These assumptions are listed below.

Assumptions regarding humidity

When discussing humidity, it was necessary to make several assumptions. Most humidity sensors have a response time of several seconds. This is acceptable for basic applications but not for breath analysis. Given that the respiratory rate typically ranges between 12 and 20 breaths per minute [15], it can be inferred that a single breath, comprising exhalation and inhalation, lasts for approximately 3 to 5 seconds. Therefore, in order to accurately track the humidity curve during exhalation, a very fast humidity sensor is required. Multiple research papers are available on ultra-fast humidity sensors for breath analysis, but these sensors are hardly commercially available. Therefore, it was decided to continue using the current humidity sensor, SHT41, despite its slow response time to humidity of 4 seconds.

As the humidity sensor used cannot precisely measure humidity changes during a breath, it was assumed that humidity rises rapidly during exhalation and remains constant throughout. During inhalation, the humidity level decreases to ambient. Thus, the humidity curve was assumed to have a rectangular shape. This statement is based on the results from Scheenstra et al. [43]. In this paper the humidity of tracheal gas over two breaths is visualised. The shape of the curve can be approximated by rectangles.

Another assumption was that the maximum humidity remains constant over several breaths. A visualisation of the assumptions made in this context is shown in Figure 23.

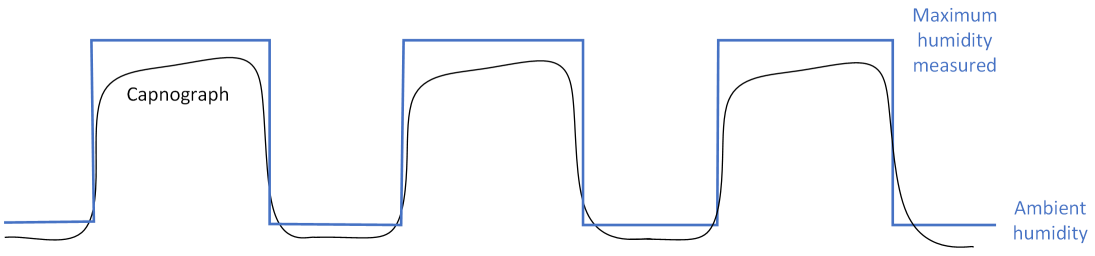

Figure 23: Visualisation of the made assumptions. The black line shows a capnograph and the blue line the assumed humidity curve over several breaths. The humidity stays constant over each breath cycle. As the maximum humidity value the maximum measured humidity over all breath cycles is used.

As the humidity sensor used is not fast enough to determine the maximum humidity of each breath, the overall maximum was used to set the amplitude of the rectangle. During the performance of a breathing test on the TC sensor, whereby the sensor was subjected to multiple breaths in succession, the humidity was concurrently measured. Subsequent to the completion of the breath measurement, the maximum humidity value was determined during post processing. The statement is based on findings from Mogera et al. [44]. This paper presents the measurement of the humidity curve during several breathing cycles. Based on these measurements, it can be concluded that humidity only changes slightly over several breaths.
The expected values for exhaled breath humidity range from 90 to 100 %.

Assumptions regarding temperature

Similar to the humidity measurements, the temperature sensor is also too slow to display the temperature curve during exhalation and inhalation. Thus, it was assumed that the temperature curve follows a rectangular sequence. This assumption is based on Mogera et al. [44], who measured the temperature curve over two breaths, which led to the aforementioned assumption.
The temperature sensor exhibits a faster response time than the humidity sensor. Consequently, unlike the humidity sensor, the temperature sensor is able to measure the maximum temperature of each breath. As a result, the amplitude of the temperature rectangle was determined by the maximum temperature measured for each breath. Figure 24 visualises the assumptions made for the temperature compensation.
The expected maximum temperature is around 35°C.

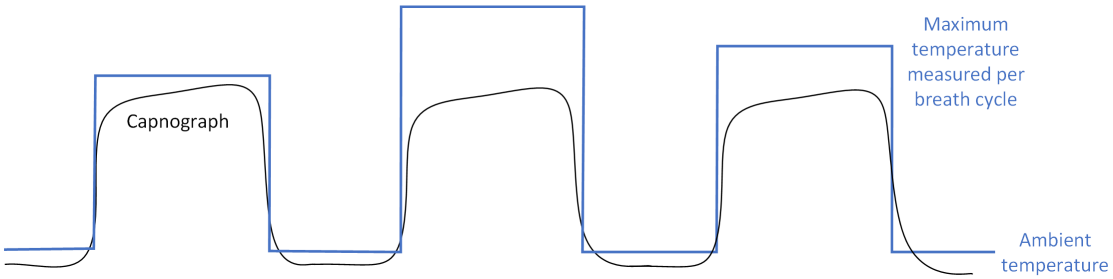

Figure 24: Visualisation of the made assumptions. The black line shows a capnograph and the blue line the assumed temperature curve over several breaths. The temperature stays constant during each breath cycle.

Assumptions regarding pressure

During respiration, there are no pressure differentials. Therefore, no assumptions needed to be made for pressure sensing. The pressure was measured to enable conversion from the unit per cent to mmHg.

Assumptions for compensation

The compensation algorithm takes into account both temperature and humidity. The thermal conductivity shows a linear dependence on temperature, with the slope of the temperature dependency varying depending on the gas, as shown in Figure 12.
The thermal conductivity is linearly dependent on humidity only within a certain temperature range. However, in the area of the expected maximum temperature, the thermal conductivity still shows a linear dependence on humidity. However, at higher temperatures, the dependence becomes non-linear.

Flow chart of the compensation algorithm

The flowchart of the compensation algorithm is shown in Figure 25 below.

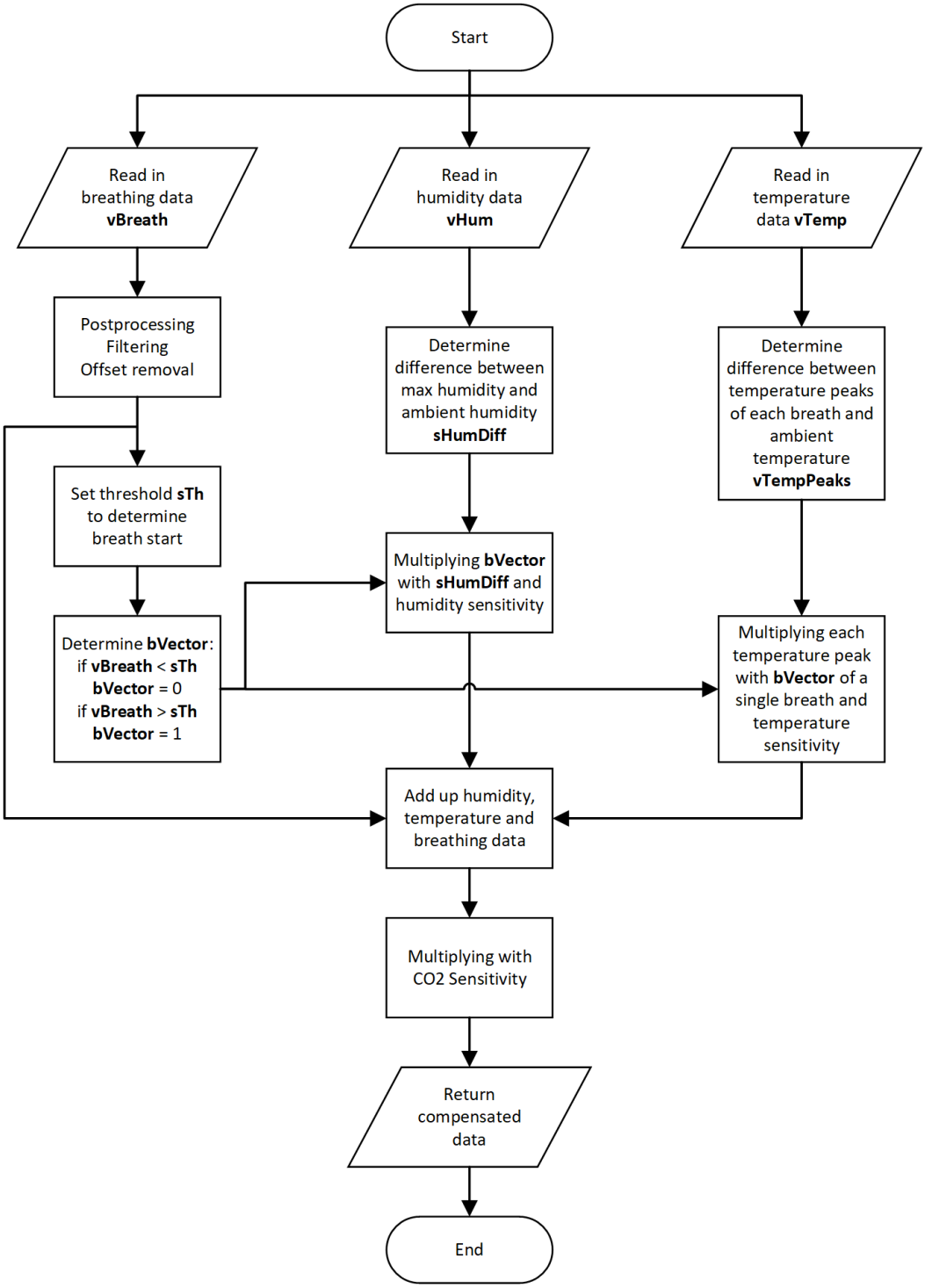

Figure 25: Overview of the flowchart of the compensation algorithm

2.10 Application tests

To measure the data required to determine the dynamic CO_2 curve, subjects breathed calmly and regularly through a tube onto the TC CO_2 sensor and the Sensirion SHT41 humidity and temperature sensor. Figure 26 shows the setup that was used.

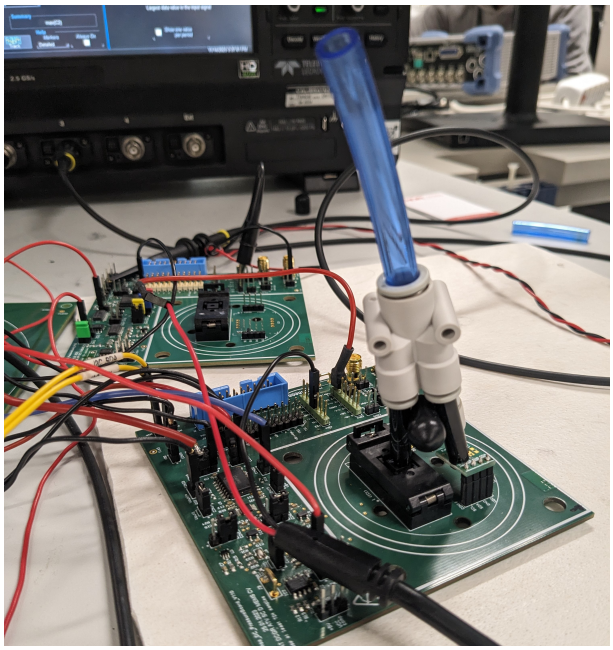

Figure 26: Used setup to perform the capnography. The exhaled breath is transported to the CO_2 sensor and the SHT41 through the tubes.

The response of the sensor to different levels of CO_2 was tested through deliberate hyperventilation and hypoventilation.
Additionally two subjects were measured both when healthy and when sick to demonstrate corresponding sensor reactions. The first subject presented with symptoms of a cold and fever. The second subject complained of shortness of breath and exhibited signs of acute bronchitis.
The concentration of CO_2 was expressed as a percentage, which is not common in medicine. In order to be consistent with standard medical practice, the percentages were converted to mmHg using the Formula 33:

$$\text{c in mmHg} = \frac{\text{c in \%}}{100} \cdot P_{ambient} \tag{33}$$

c is the concentration, $P_{ambient}$ is the ambient pressure in mmHg.

3 Results and Discussion

The following part presents the results obtained during the thesis. Throughout, the results are interpreted and discussed. The section initiates with a characterisation of the CO_2 sensor sample that was utilized. Subsequent to this, the findings obtained through the usage of the 3 omega method are presented. Following this, a determination of the CO_2 sensitivity of the sensor, as well as its reliance on humidity and temperature, is conducted. The dynamic CO_2 curve while breathing was determined using an algorithm, that takes into consideration all the acquired information. The results of the application are subsequently documented.

3.1 Characterisation of CO_2 Sensor

In course of the initial characterisation of the CO_2 sensor, the thermal time constant τ and the resistance were obtained using the hot wire method. This was done by applying a voltage pulse to the sensor and measuring the transient response. The thermal response of the sensor is shown in the following Figure 27.

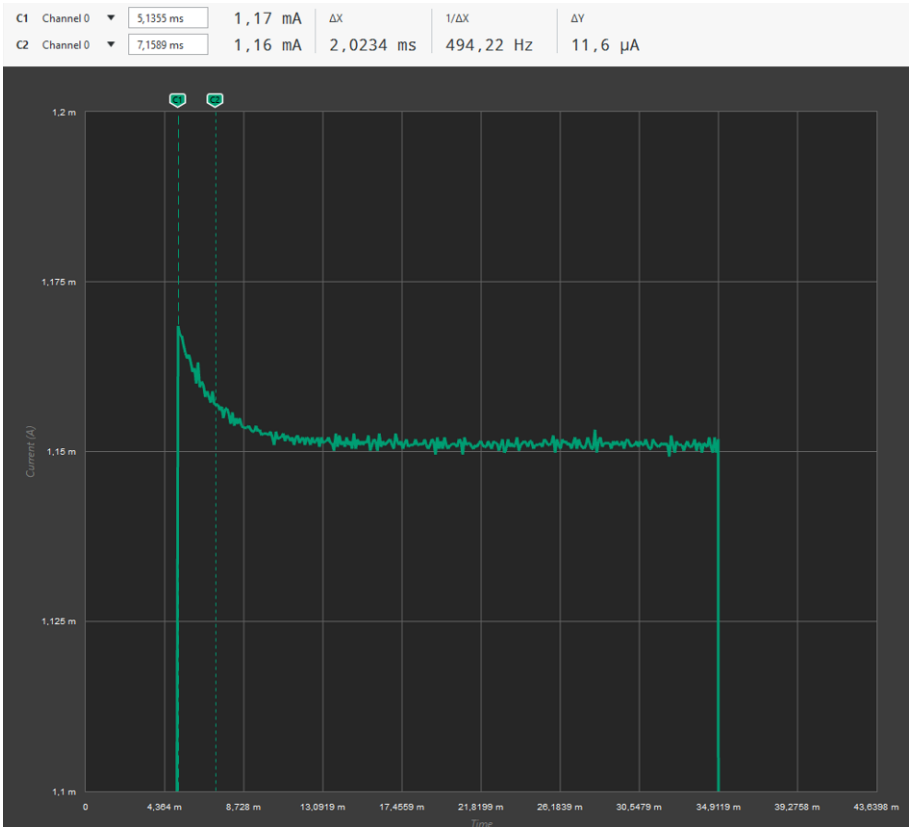

Figure 27: Measured transient response of the CO_2 sensor. The measured current follows an exponential course. The time difference between the maximum current and the current, when it is decreased to 37% of ΔI between the maximum and the end value of the current, is the thermal time constant τ

The figure above shows that the transient response follows an exponential curve. The thermal time constant τ could be determined by using two cursors. The thermal time constant τ is the time difference between the maximum current measurement and the point at which the current has dropped by 63% of ΔI between the maximum and the end value of the current. In this case, τ has a value of 2 ms.

Another value which was determined is the steady state resistance of the sensor. The measured resistance is equal to 4.26 kΩ. Applying Ohm's Law to the measured current 1.17 mA and applied voltage 5 V yields the same resistance.

3.2 3 Omega Method Simulation and Measurement

Prior to performing any measurements, a simulation was conducted using the 3 omega method on a single wire sample. It is important to note that the resistance and thermal time constants of the single wire sample deviate from those in bridge configuration. However, a single wire sample is sufficient to demonstrate the suitability of this measurement principle for the intended application.

3.2.1 Validation of the Simulation

In order to ensure the accuracy and reliability of the simulation, its results are compared with various points in the existing literature [6] and [30]. The simulation should align with these points to ensure its validity:

- Sensitivity decreases as frequency increases
- At low frequencies, the temperature oscillations are higher
- Gases with a high thermal conductivity, such as H_2, reduce the amplitude of the temperature oscillations ΔT
- Gases with low thermal conductivity, as such CO_2, increase the amplitude of the temperature oscillations ΔT

The simulation was performed for several frequencies, so that the results can be plotted over frequency. The results compromise the amplitude of the temperature oscillations ΔT. The results for three different gas compositions, air, 2.5% H_2 in N_2 and 100% CO_2, are visualised in Figure 28.

The figure displays the change in temperature ΔT as a function of frequency. The thermal conductivity of 2.5% H_2 is higher than that of air, resulting in a smaller ΔT. For 100% CO_2, the ΔT is higher because the thermal conductivity is lower. The sensitivity decreases with increasing frequency as the deviation for ΔT of 2.5% H_2 and ΔT of 100% CO_2 to ΔT of air decreases.

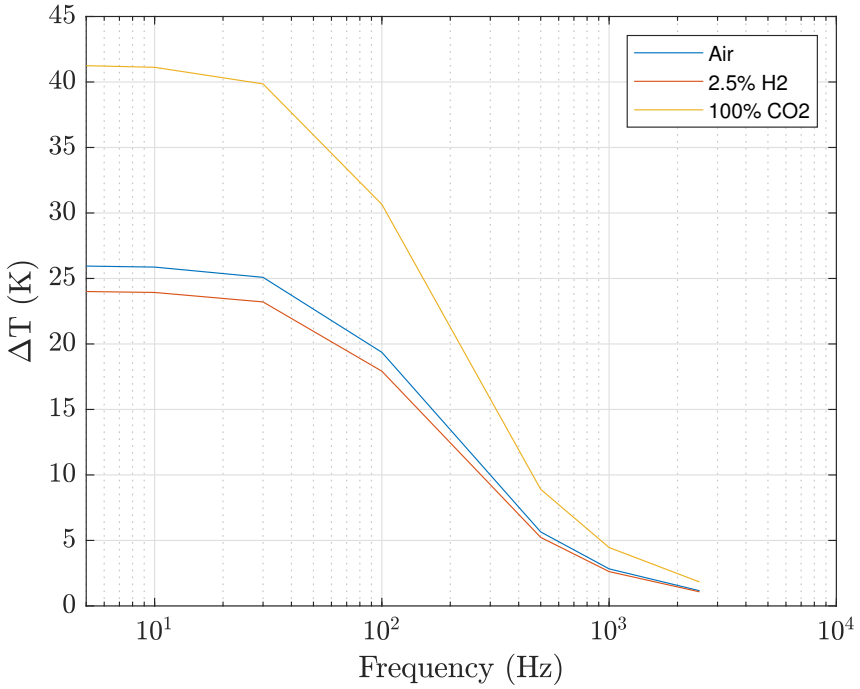

Figure 28: Simulation results showing the amplitude of the temperature oscillation ΔT for different thermal conductivities.

3.2.2 Measurement Results

The subsequent graph, Figure 29, represents the temperature amplitude curve ΔT over frequency for air and 2.5% H_2 measured with the available setup. The curve displays similarities to the curve of the simulation, as shown in Figure 28. A notable discrepancy is observed in the ΔT values at low frequencies in the simulation, where the air value is approximately 26 K, while the measurement value is approximately 18 K. This discrepancy can be attributed to several factors. Firstly, the constant resistance is neglected in the simulation, resulting in a higher power being applied to the sensing resistance. Secondly, the simulation does not consider additional heat losses, assuming that the heat transfer is only in one direction.

Additionally, it is evident that the difference in ΔT between air and H_2 is minimal in the measurements. This is attributed to the fact that the wire does not heat significantly.

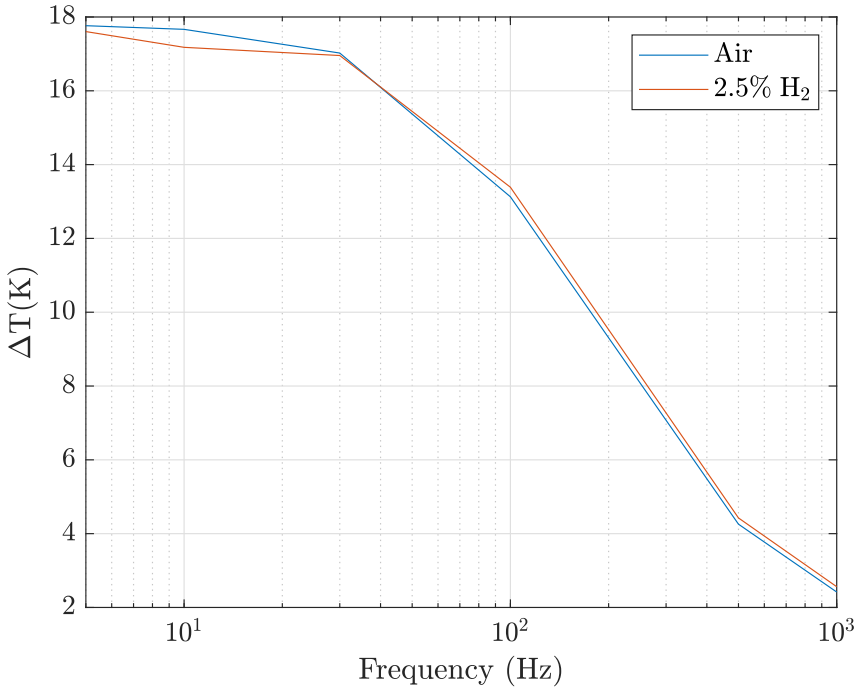

Figure 29: Measurement results showing the amplitude of the temperature oscillation ΔT for different thermal conductivities of air and 2.5% H_2.

Figure 29 also illustrates that, from 30 Hz onwards, the ΔT of H_2 is higher than that of air. This is contrary to expectations, given that the higher thermal conductivity of H_2 would result in better heat conduction, leading to a decrease in ΔT. The reason for this discrepancy is the configuration of the setup. Even at low frequencies, the difference in ΔT between air and H_2 is minimal. As frequency increases, the ΔT difference decreases. The setup is not precise enough to measure this deviation. The main problem is that the data acquisition was performed using an oscilloscope. Here, the entire bandwidth was used to acquire the signal, which resulted in the introduction of a significant amount of noise into the measurement. Additionally, the input range of the signal was wide, as not only the amplitude of the 3ω component was measured but also the entire signal, including the component at 1ω.

As the actual quantity measured is the voltage $V_{3\omega}$ and not ΔT, the measured voltage deviation between the two gases is used for SNR (signal-to-noise ratio) calculations. The relationship between ΔT and $V_{3\omega}$ is shown in Formula 22. For SNR calculations, Formula 34 is used:

$$SNR = 20 \log_{10} \left(\frac{U_{eff,signal}}{U_{eff,noise}} \right) \tag{34}$$

The noise of the setup is approximately 330 μV. For the signal, the voltage difference of $V_{3\omega}$ between air and 2.5% H_2 is used.

Figure 30 illustrates the SNR over frequency. The SNR is located around to 0 dB, indicating that the measured voltage difference between the two gases is masked by noise.

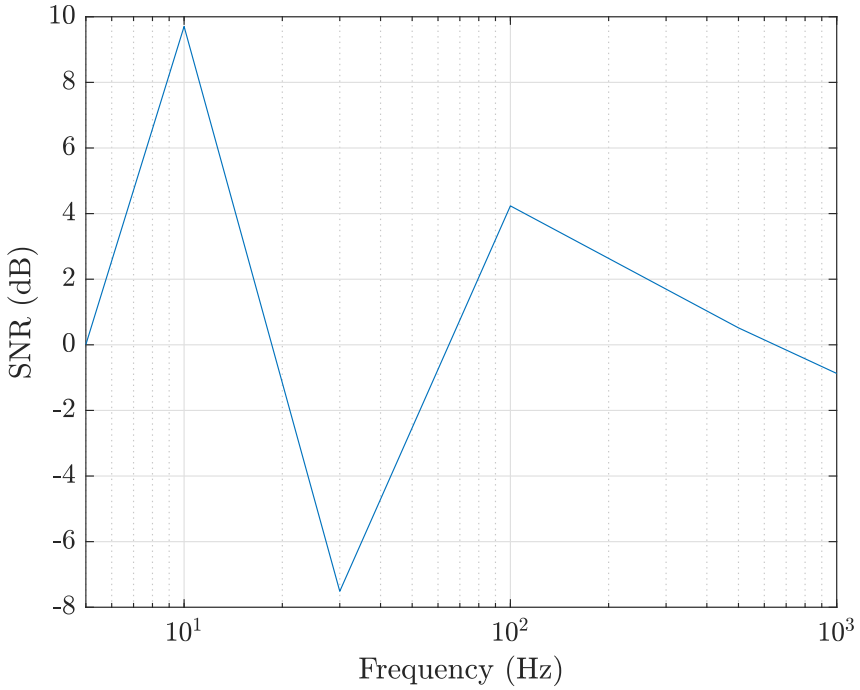

Figure 30: SNR of the voltage difference between the $V_{3\omega}$ of air and 2.5% H_2.

In accordance with the 3σ rule, 99.7% of the noise can be expected to lie within a range of three times the measured noise. This implies that the minimal measurable voltage should be approximately 990 μV in order to ensure that no noise will mask the desired signal. Upon conversion to ΔT, this results in a minimal measurable ΔT of 0.48 K.
As illustrated in Figure 29, the discrepancy between the ΔT of the two signals is too small to be accurately quantified.
Furthermore, it should be noted that the measurements were conducted using 2.5% H_2. For the intended use of measuring CO_2, even smaller deviations are expected, as the thermal conductivity of H_2 is much higher than that of CO_2.
Additionally, the signal required a period of several seconds to be acquired in order to obtain a visible third harmonic. In order to achieve a sampling time of 10 ms, it is not possible to average over multiple oscillations for a signal of sufficient quality.
In order to enhance the SNR, two possibilities exist. The first is to increase the signal itself, which could be achieved by increasing the supply current. However, this would result in a higher power consumption, which is not a desirable outcome.
The second option is to reduce the noise, which can be achieved by optimising the setup. To improve the setup, a lock-in amplifier is necessary to use. This is the standard method for conducting 3 omega measurements. The device is capable of separating the harmonics of the voltage. Nevertheless, using a lock-in amplifier is not a preferable solution,

as it results in additional expenses, which negates the cost advantages that a thermal conductivity sensor offers in comparison to other CO_2 gas sensors.

3.2.3 Comparison of 3 Omega Method and Hot Wire Method

Both the hot wire method and the 3 omega method are based on the principle that a wire heats up due to an electric current passing through it. Because of this temperature change, the resistance of the sensing element changes as well.

For the hot wire method a pulse is applied. Following from that the resistance change. The resistance change depends on the thermal conductivity of the surrounding gas. Measuring the voltage change over this sensing element, the concentration of the surrounding gas can be determined. This measurement method can be used in transient and steady state operation. In the transient operation the thermal time constant is used to obtain information about the surrounding gas. As shown in Formula 11, the thermal time constant is depending on the thermal conductivity, heat capacity and also the density.
In steady state operation, the resistance change is used to determine the concentration of the surroundings. This method has the disadvantage of being slower than the transient operation mode, as it requires waiting until the steady state is reached. The steady state is reached after 5 times the thermal time constant.
The steady state temperature and resistance values depend only on the thermal conductivity and not on any other thermal property, according to the Formula 10.

The 3 omega method offers advantages with regard to sensitivity at low frequencies when compared to the hot wire method. At higher frequencies, the hot wire method is more sensitive than the 3 omega method. Therefore, since the 3 omega method is more suitable for low frequencies, it is also a slower measurement technique compared to the hot wire method.

The parameters τ and φ of the two measurement methods are related to each other. Figure 31 illustrates the simulation between τ and φ, obtained by conducting the simulation at a frequency of 10 Hz and by setting the thermal conductivity to the thermal conductivity of 2.5% H_2.

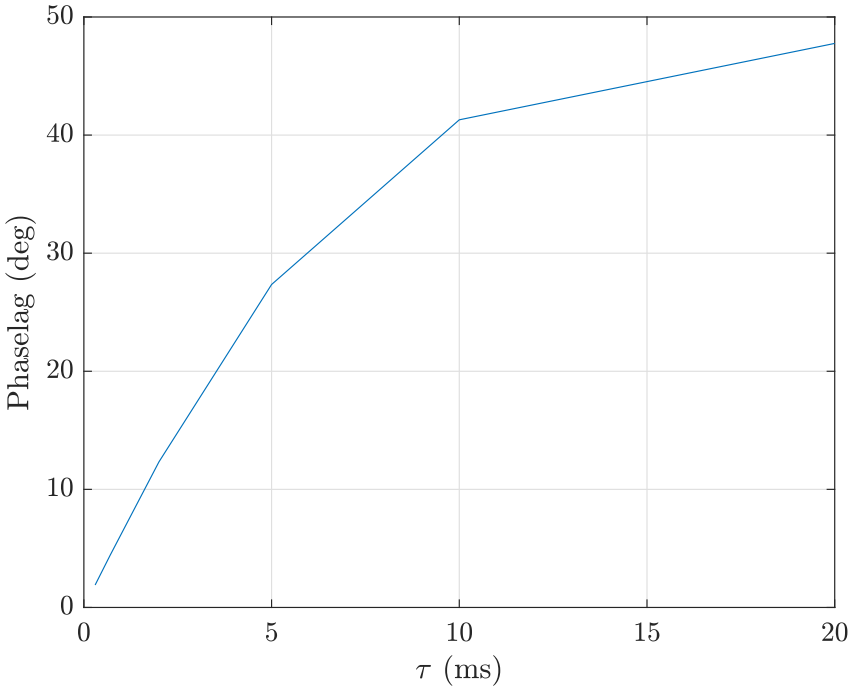

Figure 31: The result of the simulation of the relationship between the thermal time constant τ and the phase lag φ

τ is the time taken for the system to respond to a change in temperature. Using the 3 omega method, the time taken for the system to react to a change in temperature is described by the variable φ. As the τ value increases, so φ also rises, reflecting the fact that the thermal system takes longer to respond to a change in temperature.
At low frequencies, the system is quasi-static. In this frequency range, thermal conductivity has the strongest influence. Additionally, there are only small phase lags at these frequencies, as transient effects have minimal impact on the measured output signal.
As the frequency increases, the thermal diffusivity becomes more significant. In this frequency range, the system is no longer quasi-static, and the thermal response of the system affects the output signal. This effect is visible as the phase shift φ.
Kommandur et al. [30] suggested utilising the phase lag to determine gas concentrations. However, it is unclear whether this approach would result in enhanced sensitivity.

After considering all the advantages and disadvantages, it was decided to conduct the measurements using the hot wire method in steady state mode. Given that τ of the sample used in bridge configuration is 2 ms, a sampling time of 10 ms can be achieved. Another advantage of this method is that the steady state value depends only on the thermal conductivity and not on other thermal properties.
This measurement method was also used for the determination of the CO_2 sensitivity and the characterisation of the cross sensitivities. Later, it was also used to conduct the capnography measurements.

3.3 Noise Analysis

For the purpose of capnography measurements, the Single Dut Setup was utilised to achieve a rapid sampling time. In this setup, a sampling time of 10 ms was used. The noise level of this setup is 8.13 μV. A moving average filter is used to improve the noise performance. Due to the fast changes in the expected signal, a window size of 10 is chosen. By applying this filter in post processing, the noise is reduced to 3.18 μV. The findings are also summarised in Table 3.

Table 3: Noise of the Single Dut Setup

	Noise σ (μV)
no filter	8.13
moving average filter windowsize = 10	3.18

The noise in this setup is composed of the voltage source noise σ_{Vs}, the bridge circuit noise σ_{R}, and the MEIF noise σ_{MEIF}. There are additional electrical components that contribute to the overall noise. However, they have not been included in the noise analysis as they are all low noise.

$$\sigma = \sqrt{{\sigma_{MEIF}}^2 + {\sigma_R}^2 + {\sigma_{Vs}}^2} \tag{35}$$

The noise of the bridge circuit depends on the Boltzmann constant ($\mathrm{k_B}$), temperature (T), bridge resistance (R), and bandwidth (B). The bandwidth of the MEIF is 10 kHz. The resistance noise is calculated as follows:

$$\sigma_R = \sqrt{4 k_b T R B} \tag{36}$$

$$\sigma_R = \sqrt{4 \cdot 1.38 \cdot 10^{-23} \cdot 300 \cdot 4260 \cdot 10^4} = 0.84\ \mu V_{RMS} \tag{37}$$

The noise from the signal source has little impact on the overall noise as it is cancelled out by the Wheatstone bridge circuit. Thus, σ_{Vs} is assumed to be close to 0, the noise of the MEIF can be calculated according to Formula 35.

$$\sigma_{MEIF} = \sqrt{\sigma^2 - {\sigma_R}^2} = 8.08\ \mu V_{RMS} \tag{38}$$

The main contributor to the noise is the MEIF. The determined noise is equivalent to that of the MEIF noise, which is known. As the MEIF was designed for a different application, there is room for improvement in this area. By adapting the technology to this specific application, the noise performance could be improved.

The amplifier utilised in the MEIF is a chopper amplifier, which results in a relatively low 1/f noise. As the majority of the main components are situated within the low-frequency range, the implementation of a low-pass filter could also serve to improve the noise.

3.4 CO_2 Sensitivity Determination

After performing the measurement for the CO_2 sensitivity determination, the data obtained was processed, evaluated, and visualised in MATLAB R2020b. The CO_2 sensor output was filtered during post processing using a moving average filter with a window size of 100. Table 4 shows an overview of the noise improvement achieved by the filter. The standard deviation was used to determine the noise. The application of a moving average filter to the measured data resulted in a reduction of noise by a factor of 10. Given that the expected CO_2 sensitivity was set to 60 μV/%CO_2, a noise level of 14 μV could significantly affect the signal. Therefore, filtering is crucial. The use of a filter with a large window size inevitably results in a slower sampling time. However, these parameters were employed solely for the determination of CO_2 sensitivity, with the objective of ensuring an accurate result.

Table 4: Noise of the DevKit

	Noise (μV)
no filter	14.3
moving average filter window size = 100	1.43

The primary sources of noise in this setup are the quantisation noise of the ADC as the differential bridge voltage is not being pre amplified.
The reference CO_2 sensor, the GMP343, was used to measure the CO_2 concentration within the pressure chamber. In Figure 32 the filtered output of the DevKit and the GMP343 data are shown.
The output voltage of the DevKit is shown on the left hand y-axis and the concentration of CO_2 in the pressure chamber is shown on the right hand y-axis. From t_0 to t_1 the CO_2 concentration is set to 500 ppm, from t_1 to t_2 it is set to 1500 ppm, from t_2 to t_3 it is set to 3000 ppm and from t_3 to t_4 it is set to 6000 ppm.
It is evident that the output voltages increase as the concentration of CO_2 increases. Although CO_2 has low thermal conductivity similar to air, the sensor is sensitive enough to detect changes in CO_2.

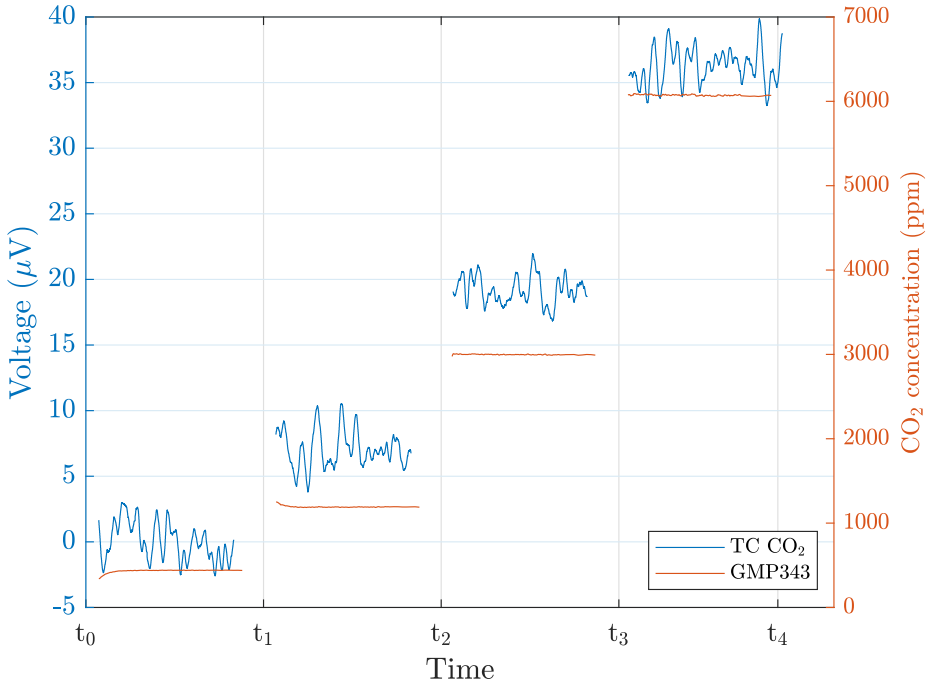

Figure 32: The left hand y-axis shows the measured and filtered output voltage of the DevKit. The right hand y-axis shows the measured CO_2 value within the pressure chamber. The output voltages increases, with increasing CO_2.

To determine the CO_2 sensitivity of the TC sensor, a linear fit was utilised. The mean value of the output voltage of the DevKit and the mean value of the measured CO_2 data from the GMP343 per concentration step were used to determine the value. Figure 33 displays the resulting data points and the linear fit. In this figure the mean value of the measured data of the GMP343 for each concentration step is plotted on the x-axis and the mean value of the output voltage of the of the TC CO_2 sensor on the y-axis.
The sensitivity of the TC CO_2 sensor is indicated by the slope of the fit of the data points. The determined sensitivity to CO_2 is $63\mu V/\%CO_2$. As illustrated in Figure 33, the data points do not lie precisely on the line of the linear fit. Especially the data points at 500 ppm and 3000 ppm have the largest deviation from the fit. It should be noted that the measured output voltage of the TC CO_2 sensor may have been influenced by cross sensitivities. Although the pressure chamber aimed to maintain constant conditions, slight variations may still occur. Over the measurement time, the humidity decreased from 33.8% to 28%, while the temperature remained relatively stable. The temperature exhibited a minimal change of 0.3°C from the start to the end of the measurement.
Although the ambient conditions are not entirely stable, the determined sensitivity falls within the expected range of 60 $\mu V/\%CO_2$.

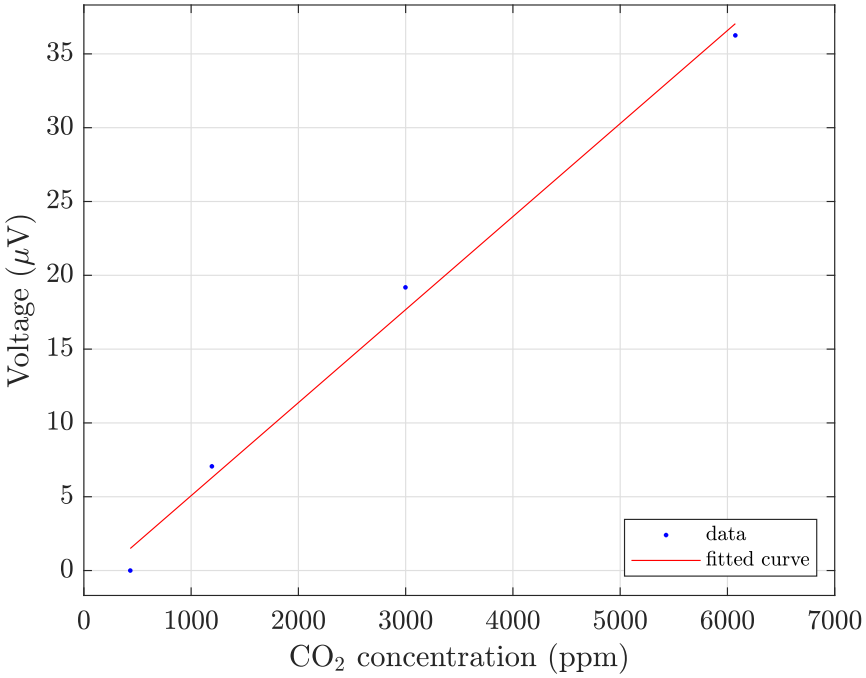

Figure 33: The data points and the linear fit. For each concentration step the mean values of the obtained data is used. The obtained sensitivity is equal to 63 μV/%CO_2.

In order to determine the concentration of CO_2 from the measured output voltage of the TC sensor, the coefficients determined by the linear fit are employed. The coefficients comprise the CO_2 sensitivity and a offset. The conversion between voltage output of the TC and CO_2 in ppm is illustrated in Formula 39.

$$CO_2 = \frac{\Delta V}{CO_2\ sensivity} = \frac{\Delta V}{0.0063} \tag{39}$$

The resulting data is then plotted alongside the measured GMP343 data, as shown in Figure 34.

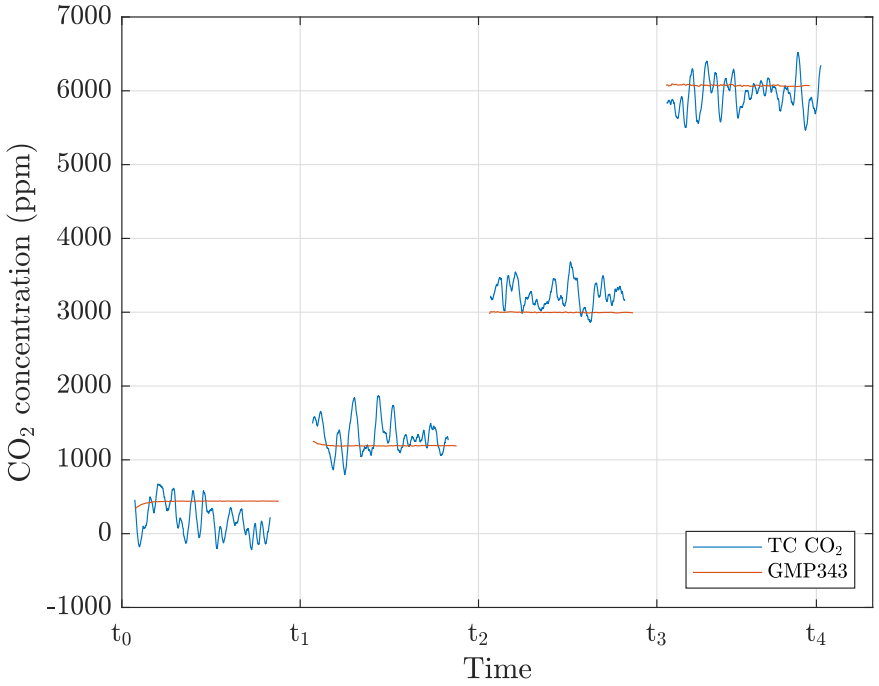

Figure 34: Calculated and measured CO_2 concentration. For calculation the output voltage of the TC sensor and the determined CO_2 sensitivity is used.

The figure above shows that the concentration determined at 500 ppm and 3000 ppm deviates the most from the reference concentration. Compared to the GMP343, the TC CO_2 sensor exhibits significant fluctuations.

To demonstrate the accuracy of the data, the mean CO_2 concentration determined by the TC sensor is compared to the mean of the reference values. The SNR for the various concentration steps has also been determined. In order to perform the SNR calculations, the Formula 34 is employed. In order to obtain the SNR of the TC sensor, the mean value of the corresponding concentration step, measured by the TC and subsequently converted into ppm CO_2, is employed. The noise level in ppm is calculated using the value of the filtered noise from Table 4, resulting in a noise level of approximately 227 ppm. For the conversion from the output voltage of the TC sensor to CO_2 in ppm Formula 39 is used. Furthermore, the SNR for the reference sensor GMP343 is calculated using Formula 34. The obtained results are listed in Table 5.

Table 5: Summary of the set CO_2 concentrations, the concentrations measured by the TC sensor and the GMP343 reference sensor. Furthermore, the SNR for the filtered data is determined for each concentration step.

set CO_2 (ppm)	mean(TC) (ppm)	mean(GMP343) (ppm)	SNR of TC (dB)	SNR of GMP343 (dB)
500	195.66	432.74	-1.31	27.27
1500	1315.69	1193.58	15.48	40.58
3000	3239.24	2998.18	25.71	57.21
6000	5947.57	6073.67	28.92	57.80

The noise level of the TC sensor remains consistent across various CO_2 concentration levels, suggesting that it has a greater impact on lower concentrations, such as 500 ppm. At this concentration level, the mean of the data measured with the TC sensor displays the largest relative difference to the actual CO_2 value measured by the GMP343. The noise at this concentration step is higher than the actual measured signal, resulting in a negative SNR.

Upon examining the other concentration steps, it is evident that the difference between the mean of GMP343 data and the mean of the TC sensor data decreases as the CO_2 concentration increases.

Furthermore, the SNR improves as the concentration of CO_2 increases, since the noise remains constant throughout the concentration steps.

The SNR of the reference sensor is superior to that of the TC sensor, as the noise of the GMP343 is considerably lower than that of the TC sensor, with a standard deviation of approximately 10 ppm. Furthermore, the SNR of the GMP343 also increases with increasing concentration.

The results indicate that the TC sensor is not appropriate for measuring low concentrations, such as monitoring ambient CO_2 levels, because the noise level is around 200 ppm. However, as the intended use is for breath analysis, where CO_2 concentrations ranging from 3.8% to 5.2% (38000 to 52000 ppm) are expected, the level of noise is not a significant concern. The deviation from the TC data to the GMP343 data also decreases as the CO_2 concentration increases. Therefore, the TC sensor is more suitable for applications with higher CO_2 concentrations, such as capnography.

To enhance the SNR and enable a TC sensor to measure low concentrations of CO_2, additional averaging is necessary. However, this results in a longer sampling time.

3.5 Cross Sensitivities

Each cross sensitivity has a unique effect on the output signal. The presence of a parasitic effect can cause either an increase or a decrease in the signal.
As previously demonstrated, an increase in CO_2 results in a rise in output voltage. CO_2 has a lower thermal conductivity than air. Therefore, the heat generated by the current passing through the wire cannot be released to the surroundings effectively. As a result, the resistance increases, and a higher voltage is measured.
Humidity causes a decrease in signal due to its higher thermal conductivity compared to CO_2 and air. When humidity is present in a gas mixture, the thermal conductivity of the mixture increases, resulting in a decrease in voltage. This statement is only applicable to temperatures smaller than 70°C. A capnograph is operating within this range.
The dependence of the signal on the temperature is influenced by the humidity of the surroundings.

3.5.1 Humidity Characterisation

During the process of characterising humidity, a humidity step was applied to the TC sensor. This measurement was repeated 15 times. The resulting humidity was measured with the Sensirion SHT21. The measured relative humidity for the step ranged from 14.6% to 79.9%.
Figure 35 shows the response of the TC sensor to the humidity step. The average of 15 measurements is shown by the bold blue line in the graph. The averaging process reduces the noise and removes the outliers. The repeatability of the measurement is also shown.

Dry air was applied to the TC until time t_1. The output voltage is 0 μV as it was scaled to this value to better visualize the difference in humidity. At time t_1, the solenoid valve opened, and the humid air came into contact with the TC sensor. The response to humidity is rapid, with an output voltage of approximately -90 μV. As temperature is a crucial factor, efforts were made to maintain a constant temperature. The measurements were repeated consecutively in the laboratory under controlled conditions with minimal variation.

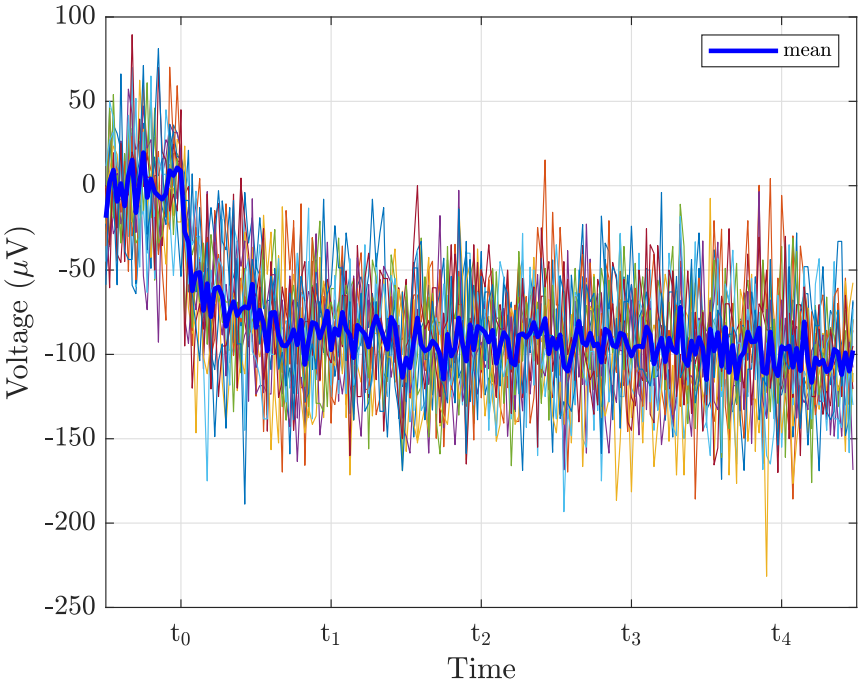

Figure 35: The response of the TC sensor to a humidity step is shown. Dry air was exposed to the TC sensor up to t_1. Starting from t_1, the response of the TC sensor to the humidity is shown. The blue line represents the mean of 15 measurements.

The data measured with the TC sensor is then further used to determine a lineaer fit between the data at dry air and the data at humid air. For the dry air, the mean was determined from the data up to t_1. For the humid air, the mean of the data from t_2 to the end of the signal was used, as the signal has had enough time to stabilise from t_2 onwards.

Although only two measurement points (dry and humid air) were taken, a linear fit was used, as at room temperature, where the measurement was conducted, the thermal conductivity rises linearly with increasing humidity.

The slope of the resulting line represents the sensitivity of the sensor. The sensitivity of the sensor to humidity was found to be $-1.4\ \mu\mathrm{V\%rH^{-1}}$. As anticipated, the result has an inverse sign to the CO_2 sensitivity, as humidity enhances the thermal conductivity.

Subsequently, the sensitivity to humidity was validated through the conduct of a measurement in a climate chamber, which enabled the generation of a humidity sweep.

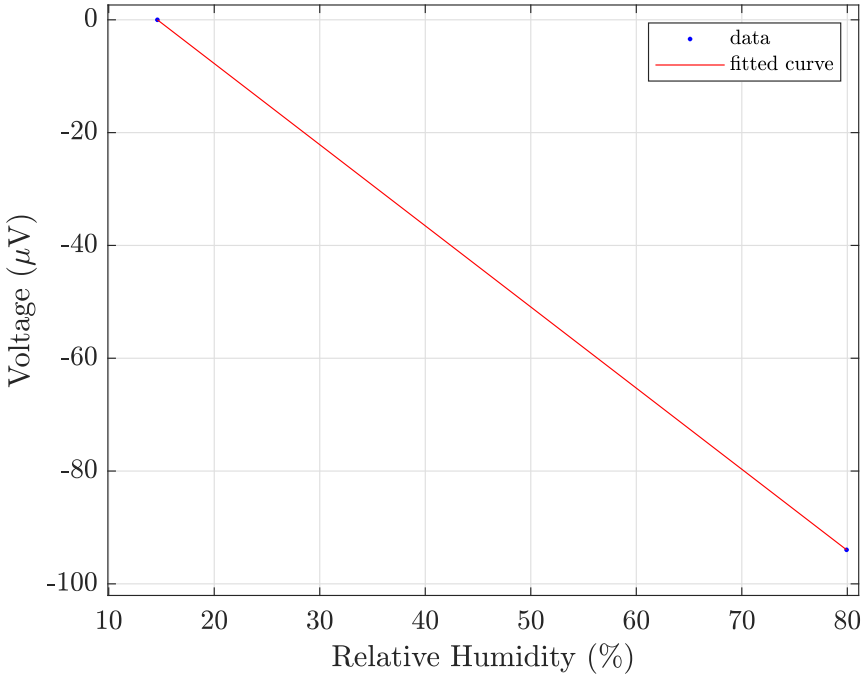

Figure 36: Data points and the linear fit of the humidity characterisation. For the dry air and the humid air the mean values of the obtained data was used. The obtained sensitivity is equal to $-1.4\ \mu\mathrm{V\%rH^{-1}}$.

3.5.2 Temperature Characterisation

Data for the temperature dependence of the TC Sensor was already available within the company and were not reevaluated. A linear fit has already been performed on the data, and the temperature sensitivity of the sensor is known to be $10\ \mu\mathrm{VK^{-1}}$.

3.6 Error estimation

Using a thermal conductivity sensor for capnography offers several advantages, such as fast sampling time, small size, and low cost. However, there are also disadvantages, particularly in the area of selectivity. The following section discusses and evaluates the challenges of performing capnography with a thermal conductivity sensor.

3.6.1 Selectivity

A known disadvantage of the thermal conductivity sensor is its poor selectivity. The sensor detects changes in gases, temperature, humidity, and pressure. The effects of humidity, temperature and pressure have already been discussed in previous sections and will be further analysed later.
Between inhaled and exhaled air two components change. As N_2 is the main component of air, it can be considered as carrier gas. The TC sensor detects changes in the thermal conductivity of the surrounding gas. As O_2 has a similar thermal conductivity to N_2, its changes do not affect the measured signal. The output signal is primarily influenced by changes in CO_2 levels, as the thermal conductivity of N_2 and CO_2 differs from each other. However, a change in the concentration of argon would affect the output signal. As argon remains constant during inhalation and exhalation this is not a concern.

3.6.2 Expected and Measured Output

To observe the behaviour of cross sensitivities during breathing, a breath test was performed using the SHT41. The SHT41 was repeatedly exposed to breath through a tube to verify the accuracy of the readings. The results are shown in Figure 37. The figure displays the humidity and temperature changes over several breaths. As the SHT41 has a humidity response time of 4 seconds, it is not possible to capture the humidity changes with each breath. The temperature peak of each breath can be determined.

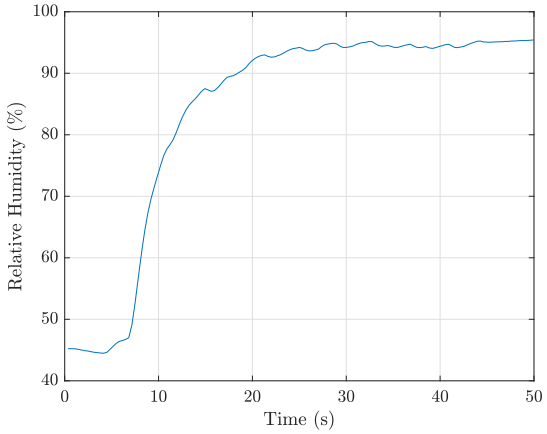

(a) Temporal changes in humidity over several breaths.

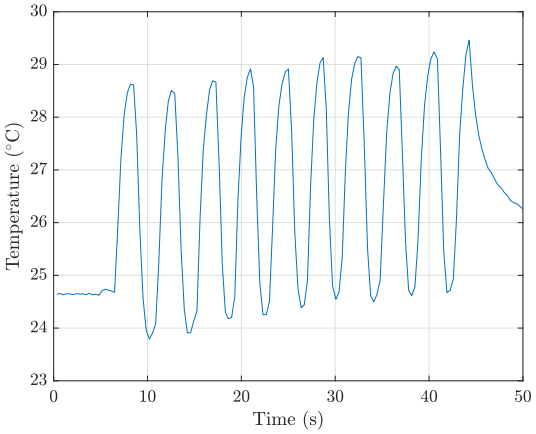

(b) Temporal changes in temperature over several breaths.

Figure 37: Figure (a) shows the temporal course of humidity over several breaths. Due to the slow response time of the sensor used, it is not possible to determine the humidity for each breath individually. Figure (b) shows the temporal course of the temperature. Here, it is possible to determine the peak temperature for each breath.

An overview of the expected and measured values is given in Table 6. For the measured values, the maximum humidity value from Figure 33 is used, which is approximately 95% relative humidity. The mean temperature peak of approximately 29°C is used to represent the temperature. Mansour et al. [16] provide the expected values for humidity and temperature.

Table 6: Overview of the expected and measured values for temperature and humidity.

Cross sensitivity	Expected	Measured
Temperature (°C)	34.5	29
Relative Humidity (%)	100	95

The measured temperature is lower than the expected temperature. Possible reasons for this could be the loss of temperature to the ambient air and the breathing tube. To verify whether the temperature also reaches the TC CO_2 sensor, the temperature was also measured with the TC CO_2 sensor. The breath measurement was repeated using the TC CO_2 sensor, and the obtained temperatures were found to be in the same range as those measured with the SHT41.

The humidity is lower than expected. Mansour [16] et al. also observed lower humidity levels than 100% in exhaled breath, and identified two potential explanations for this observation. Firstly, as temperature increases, relative humidity decreases. Secondly, the exhaled air mixes with the surrounding air.

The measured values are then set in relation to the ambient conditions. The mean value for ambient humidity and temperature is determined from the data presented in Figure 37. The first 5 seconds of data are measured under ambient conditions and can be used to determine the ambient humidity and temperature by calculating the mean during this time range. Table 7 displays the variation between the ambient conditions and the measured values, along with the anticipated alteration of CO_2 between inhalation and exhalation. The table also displays the sensitivity of each component that affects the output voltage.

Table 7: Differences between inhaled and exhaled air and the according sensitivities.

	Difference inhaled and exhaled air	Sensitivity
CO_2	5%	63 μV%$CO_2{}^{-1}$
Temperature	3.3°C	10 μVK^{-1}
Relative Humidity	50%	-1.4 μV%rH^{-1}

Table 8 shows the resulting voltages from each signal component. The voltage is calculated by multiplying the difference between the ambient and expected values by the corresponding sensitivity. The expected output voltage of the overall signal is the sum of each component.

Table 8: The calculated voltage of all components affecting the output voltage and the total output voltage.

	Calculated Voltage (μV)
CO_2	315
Temperature	33
Relative Humidity	-70
Sum	278

The primary contributor to the overall signal is CO_2, followed by humidity and then temperature. The voltage of interest is the CO_2 voltage, which measures 315 μV. However, the actual measured voltage of 278 μV is lower due to the impact of humidity and temperature.
The humidity induced voltage is -70 μV. Dividing this by the CO_2 sensitivity allows for the calculation of the impact on CO_2 output. Thus, exhaled breath humidity causes a 1.1% decrease in CO_2 readings.

Although the sensor is more sensitive to temperature than humidity, temperature has only half the impact on the output signal compared to humidity. This is because the difference between ambient temperature and measured temperature is only about 3°C. The temperature causes an increase of 0.52% in CO_2 readout.
As demonstrated, cross sensitivities significantly affect the output, making compensation essential. Despite humidity and temperature having opposite effects on the output voltage and partially cancelling each other out, compensation is still necessary. Based on estimations, the total error due to humidity and temperature would be -0.58% CO_2.

3.6.3 Precision of TC Sensor

The TC sensor noise is calculated by using the standard deviation and is 3.18 μV when a moving average filter is applied. This has an impact of 0.05% on the CO_2 output. When using 3σ, it is ensured that 99.7% of the data falls within this range around the mean value, resulting in a precision of $\pm 0.15\%$ CO_2.

3.6.4 Accuracy estimation

The accuracy of the final result depends on the humidity and temperature measurements and the uncertainties resulting from the assumptions made.

Humidity
Regarding humidity, it was necessary to make several assumptions due to the slow response time of the humidity sensor used to measure the humidity during breathing. However, as shown in Figure 37a, the humidity settles after a few breaths, and therefore the maximum value should provide a good estimation of the humidity present at the sensor. The SHT41 humidity sensor used has an accuracy of $\pm 1.8\%$ relative humidity.
However, the assumption of constant humidity throughout breathing may not always hold true. Therefore, the overall accuracy of the humidity measurement is set higher to account for these potential inaccuracies. Hence, the accuracy for the humidity measurement is set to $\pm 5\%$ relative humidity. This results in a deviation of approximately ± 7 μV or $\pm 0.11\%$ CO_2 readings.

Temperature
The temperature can be determined quite accurately. The temperature sensor of the SHT41 has an accuracy of ± 0.2°C. This corresponds to a deviation of approximately $\pm 0.03\%$ in CO_2 levels.

3.7 Capnography

Using the data obtained on the sensitivity of the TC CO_2 sensor to CO_2, humidity and temperature, capnography could be performed. The TC CO_2 sensor and the humidity sensor were exposed to multiple breaths of exhaled air through a tube. The output voltage of the Single Dut Setup was utilised for data post processing and evaluation. To reduce noise, a moving average filter with a window size of 10 was applied to the signal during post processing.

The Figure below shows the time course of the dynamic CO_2 curve over several breaths. This is the original signal without any compensations. The signal above 0 μV indicates exhalation, while the signal below 0 μV indicates inhalation.

The maximum values for each exhalation range from approximately 250 to 300 μV. The estimated output voltage is 278 μV, which lies within the measured range.

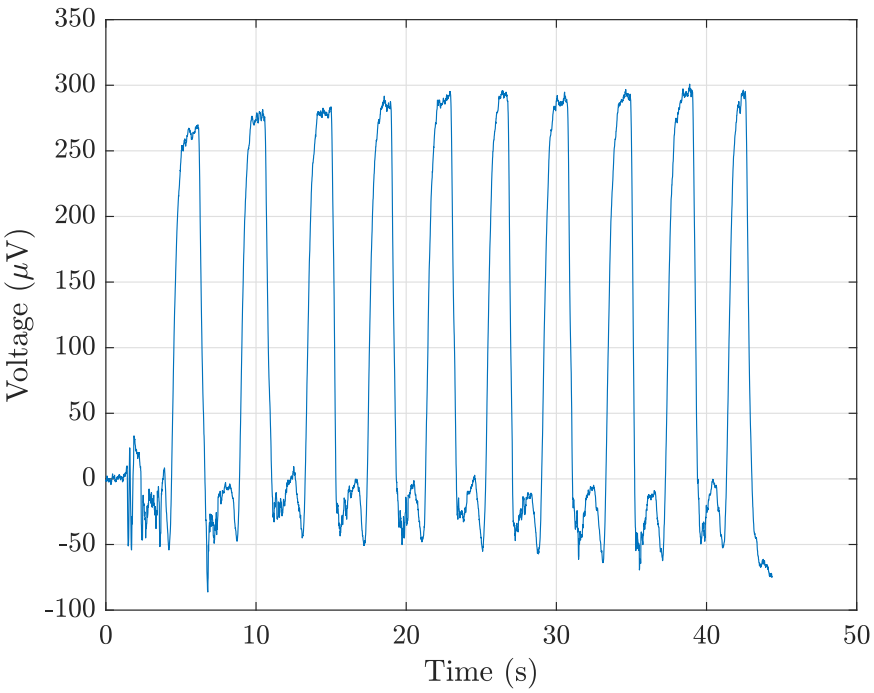

Figure 38: The time course of the resulting voltage during exhalation and inhalation over several breaths.

As shown in Figure 38, the values during inhalation are negative. This is because the humidity in the tube and at the sensor did not dissipate immediately. The remaining humidity was then detected by the TC CO_2 sensor. The signal increases during inhalation due to a decrease in humidity at the sensor.

To show the shape of the breaths and also the repeatability, each breath is plotted over each other. Figure 39 illustrates this. Here, an overall of 10 breaths is observed. The breath curves exhibit a high degree of similarity, demonstrating the repeatability of this measurement method.

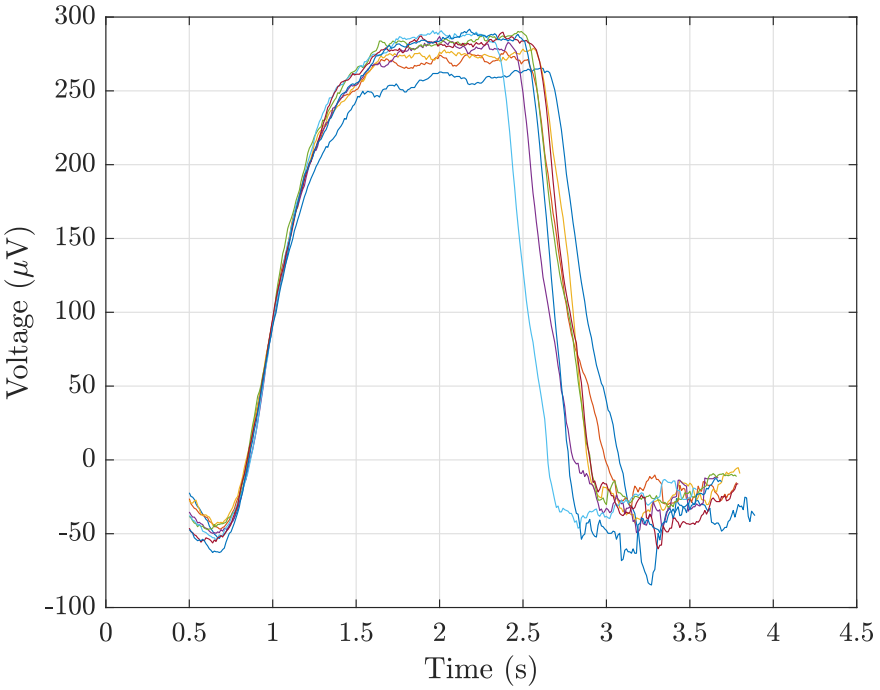

Figure 39: CO_2 curve of 10 breaths. The curves display the expiratory upstroke, the alveolar plateau, and the inspiratory downstroke. The end of the alveolar plateau represents the end-tidal CO_2 value.

The resulting curves correspond to curves found in literature. At the start of the curve, there is a brief decrease in the signal due to the exhalation of dead space air. This air does not contain CO_2, but rather humidity and a higher temperature. Thus, the humidity is measured and the signal decreases. The following phase is the expiratory upstroke. During this phase, the dead space air mixes with the alveolar gas and CO_2 is detected. The plateau phase represents the alveolar gas level. The end of the alveolar plateau represents the etCO_2 value. Following this phase, the signal experiences a rapid decrease, known as the inspiratory downstroke. The sensor only detects ambient gas, and therefore no CO_2 is detected.

3.7.1 Compensation Results

To eliminate the influence of humidity and temperature on the signal, compensation was performed. The compensation was only applied during exhalation. The humidity level during inhalation could not be accurately determined due to the limitations of the humidity sensor. Thus, only exhaled data was considered for evaluation.
Figure 40 shows the calculated CO_2 values with (blue line) and without (red line) compensation. As expected due to the influence of humidity, the compensated signal is higher than the uncompensated signal. The normal range for the concentration of CO_2 in exhaled air is between 3.8% and 5.2%. The values of the compensated signal lie within this range. The mean value over all breaths is 5.0% CO_2.

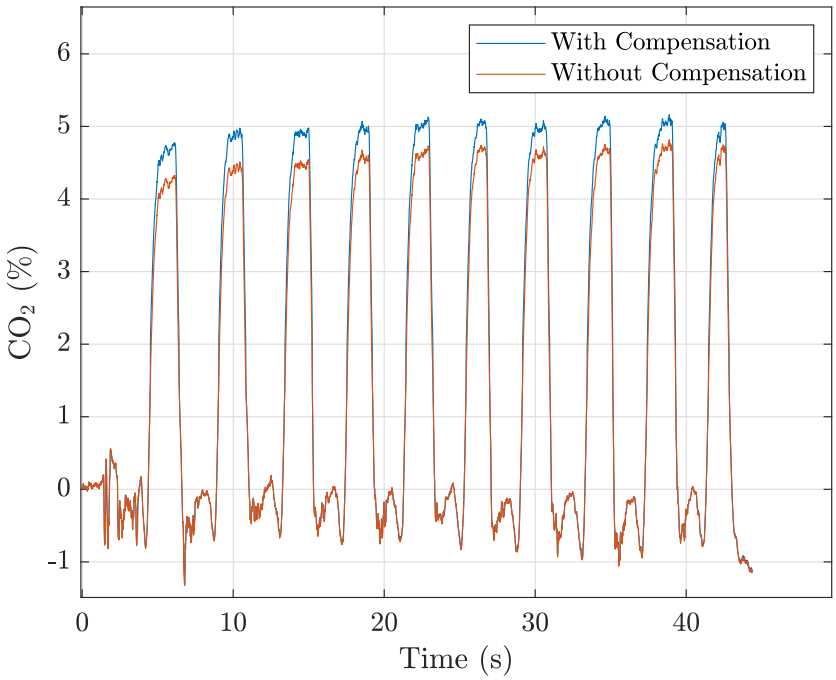

Figure 40: The time course of the compensated (blue line) and uncompensated (red line) CO_2 curve during exhalation and inhalation over several breaths.

The mean deviation between the compensated and uncompensated signals is 0.44%. This value is close to the estimated value of 0.58%.
The respiratory rate (RR) can be determined using the time course of the CO_2 curve by setting a threshold and calculating the time between reaching the threshold. The respiratory rate can be calculated as 15 breaths per minute, based on the mean breath duration of 4 seconds. This falls within the typical range of 12 to 20 breaths per minute.

3.7.2 Parameter determination

Various parameters can be used to evaluate a capnogram. The most commonly used parameter is the etCO_2 value, which represents the end value of the alveolar plateau. However, this value is not the only parameter of interest in capnography. There are also the slopes of the expiratory upstroke, alveolar plateau and the inspiratory downstroke. Also the angles between the upstroke and plateau, called α, and between the plateau and the downstroke, called β, can be used.

Figure 41 illustrates the process of determining parameters for a single breath. The slope of the expiratory upstroke was determined by calculating the slope at the inflection point of this phase. This is represented by the red line.

The black line represents a fit for the alveolar plateau phase. To determine the slope of this phase, a linear fit was carried out between the beginning and the end point of the plateau. The beginning and end of the plateau phase was determined by the algorithm proposed by Genderingen et al. [45].

The slope of the inspiratory downstroke is represented by the blue line and was determined by using the slope of its inflection point.

The angles between the phases were calculated using the linear fits. α is the angle between the red and black lines, while β is the angle between the black and blue lines.

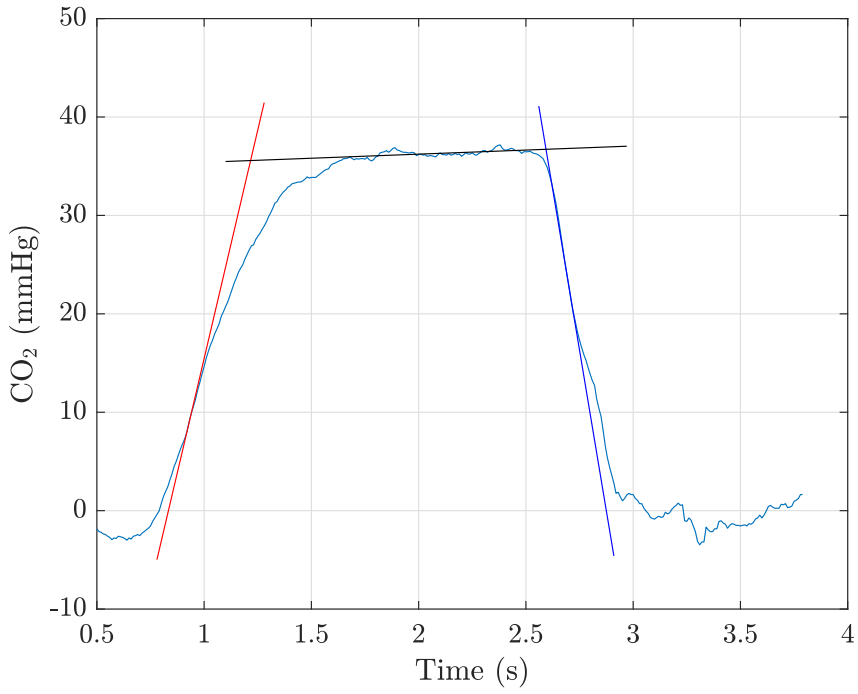

Figure 41: The time course of the CO_2 curve during exhalation and inhalation over one breath. The red line represents the expiratory slope, the black line represents the slope of the alveolar plateau, and the blue line represents the inspiratory slope.

The results of the parameter determination are compared to the data from Herry et al. [46]. Table 9 provides an overview of the data. The results were converted from percentage to mmHg to allow for comparison with literature data, as mmHg is the commonly used unit. Formula 33 was utilised for that purpose.

Table 9: Comparison of measured data with data from the literature [46]

	$\alpha(°)$	$\beta(°)$	ExSlope (mmHg/s)	InSlope (mmHg/s)	PlatSlope (mmHg/s)	$etCO_2$ (mmHg)
Calculated	138.74	116.39	92.88	-130.62	0.88	36.8
Herry et al.	139.79	90.09	126.19	-198.04	1.15	36.7

The values for the angles α and β match the data from Herry et al. [46]. D'Mello and Butani [18] state that the angle α should be around 110°. The value of 138° degrees deviates slightly from this, but is still within an acceptable range.
β is typically around 90° [18]. The calculated angle β deviates from the expected 90°. A higher angle indicates rebreathing of CO_2. This indicates a problem with the setup, as CO_2 remains in the tube and is thus rebreathed by the subject. With an optimisation of the setup, this problem should be eliminated.
The values for the plateau slope are also matching. They are also both lower than the upper limit proposed by Genderingen et al. [45] of 1.5 mmHg/s.
The expiratory and inspiratory slopes both deviate from the expected value, but are still within an acceptable range.
The peak CO_2 value, also known as $etCO_2$, falls within the expected range of 35 to 40 mmHg in both cases.

3.8 Application Results

To further validate the results of the TC CO_2 Sensor, hyperventilation and hypoventilation tests were performed. Additionally, two subjects were measured both when healthy and when sick.

3.8.1 Hyperventilation

To perform hyperventilation, the participant intentionally breathed into the tube quickly and deeply. The sensor is expected to detect a decrease in CO_2 concentration and an increase in respiratory rate.
The curve of CO_2 during hyperventilation is shown in Figure 42. The mean $etCO_2$ value is 4.4%, and the respiratory rate is 28.7 breaths per minute. It is evident that the $etCO_2$ value decreases with each breath. This is due to the fact that the body exhales more CO_2 than it produces, resulting in a decrease in the amount of CO_2 that can be exhaled.

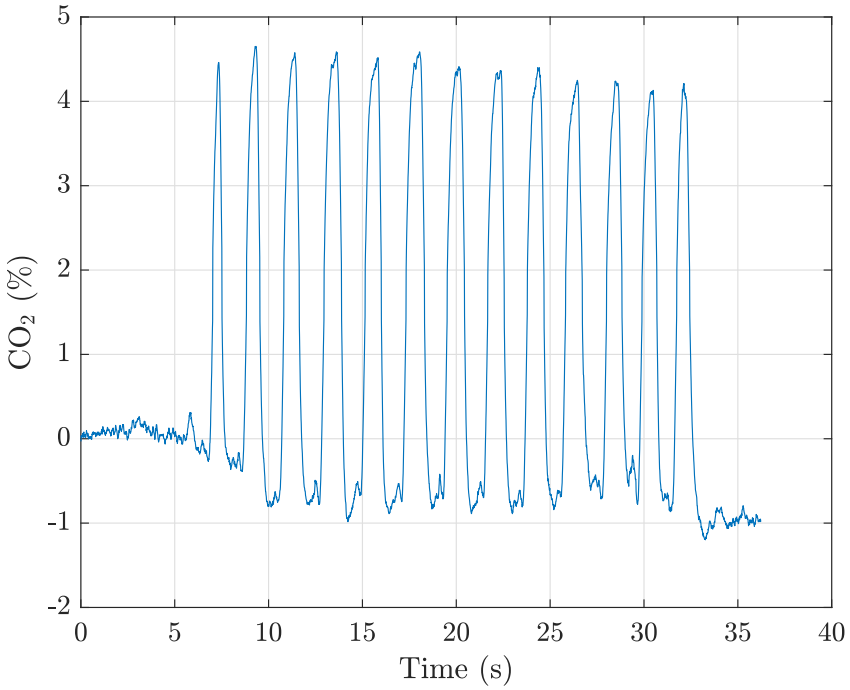

Figure 42: The time course of the CO_2 curve during hyperventilation. The measured CO_2 values are lower than during normal breathing.

3.8.2 Hypoventilation

Hypoventilation is anticipated to cause a high etCO_2 value and a low respiratory rate. To induce hypoventilation, the participant breathed slowly and flatly into the setup. The results are presented in Figure 43, with a mean etCO_2 value of 5.35% and a respiratory rate of 8.5 breaths per minute. A slight increase in etCO2 value over the breaths is observable, as the body produces CO_2 faster than it can be exhaled.

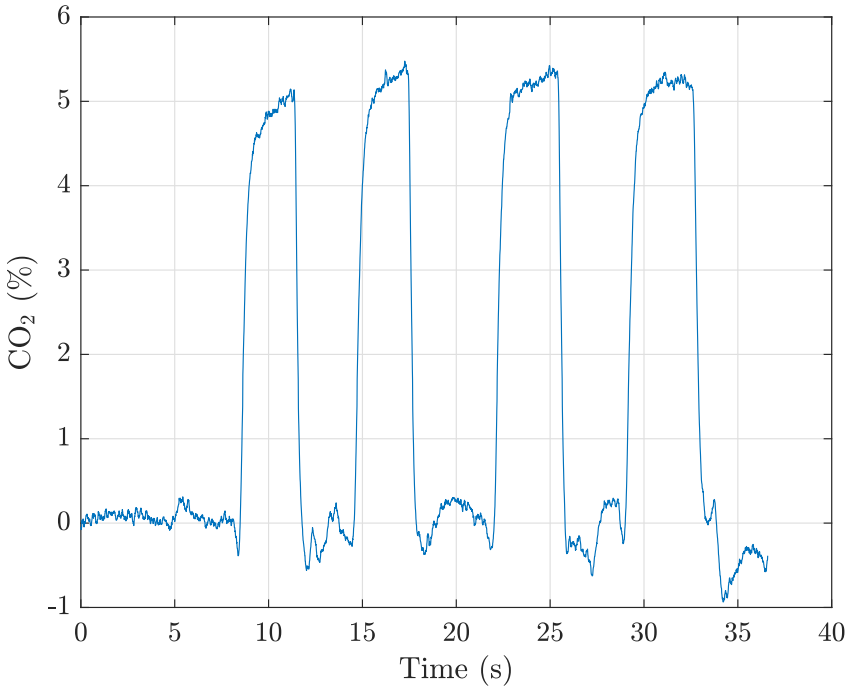

Figure 43: The time course of the CO_2 curve during hypoventilation. The measured CO_2 values are higher than during normal breathing.

3.8.3 Healthy vs Sick

During the conduction of the application testing, two subjects were monitored while ill. The first subject presented with symptoms of a cold and a fever. The second subject exhibited signs of shortness of breath and exhibited symptoms consistent with acute bronchitis. In both cases, changes in the capnograms taken during the ill periods compared to the healthy periods are evident.

Figure 44 displays the capnogram of the first subject during illness. Here, a higher $etCO_2$ value is measured compared to when the subject was healthy. The mean $etCO_2$ value is 5.7%. During fever, the body temperature increases. An increase in temperature leads to a metabolic change, resulting in an increase in $etCO_2$ levels [18]. The respiratory rate remains in the normal range at 13.3 breaths per minute.

The capnograph of the second subject deviates from the first. Here, the capnogram, as shown in Figure 45, displays an elevated slope of the alveolar plateau. This is an indicator of an obstructive disease, such as asthma and COPD. The $etCO_2$ value of 5.9% is elevated, which is typical for an obstructive disease caused by a respiratory tract infection. The respiratory rate is 18.5 breaths per minute, which falls within the normal range. Therefore, this curve indicates a temporary obstruction in the respiratory system. A week later, another capnogram was performed by the same subject and the slope had already decreased.

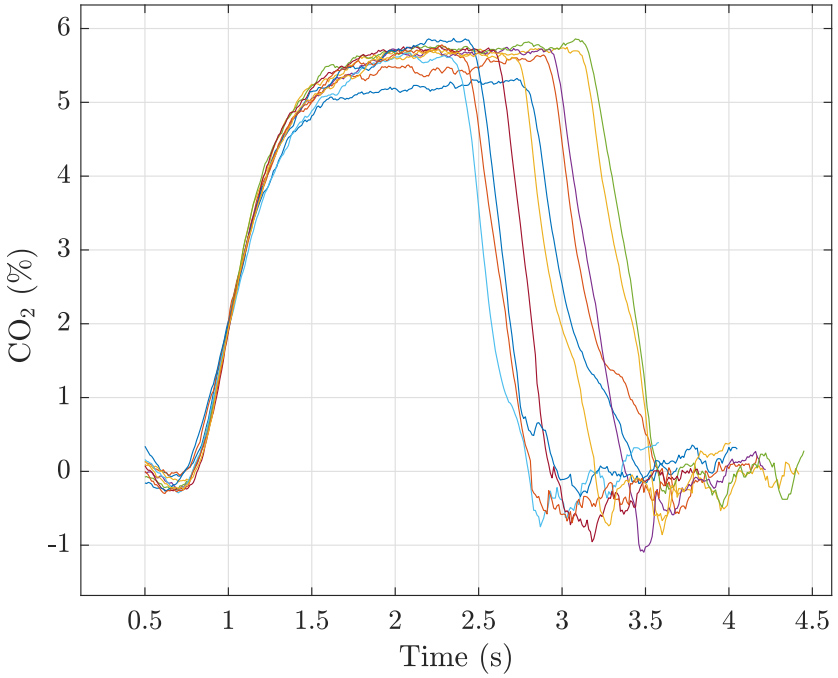

Figure 44: Shape of CO_2 curve during a fever. The etCO_2 value is elevated because of the altered metabolism resulting from an increase in temperature.

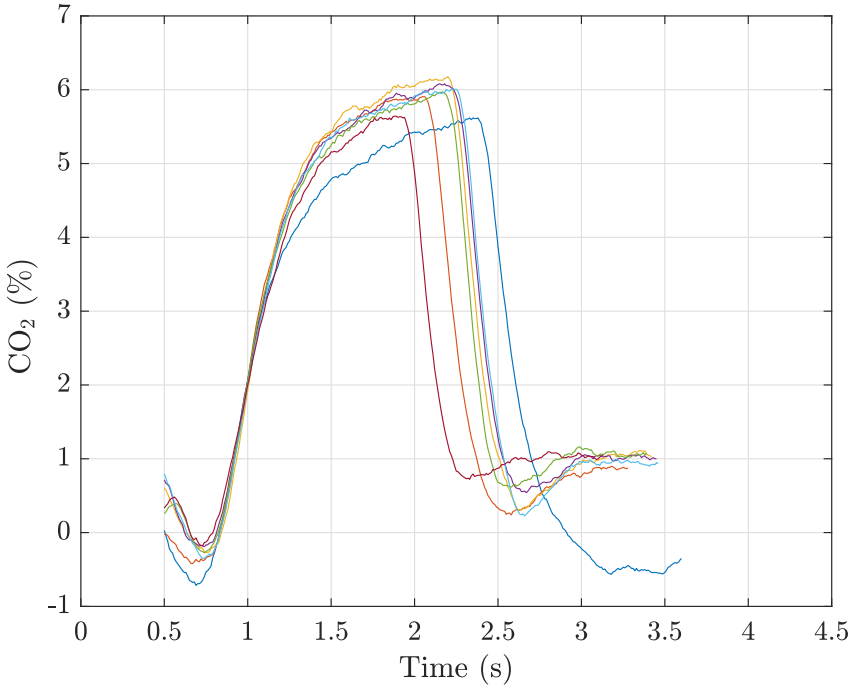

Figure 45: CO_2 curve shape during sickness. The slope of the alveolar plateau is elevated and the etCO_2 value is also elevated. The shape indicates an obstructive alternation.

3.8.4 Other possible applications

A TC CO_2 is a suitable sensor for the realisation of a capnograph for personal use, as it is small, low cost and low power. This is particularly useful for patients with obstructive respiratory diseases, such as COPD and asthma. This enables the CO_2 waveform to be measured frequently and the data to be sent to healthcare professionals. The standard method for diagnosing COPD is spirometry. However, spirometry requires the patient to exhale forcefully. Therefore, it can be challenging and tiring for patients with respiratory disease. Capnography has the advantage of being easy to use and only requiring tidal breathing. TidalSense has already conducted research in this area, demonstrating promising results in the use of capnography as a diagnostic tool [47].

4 Conclusion and Outlook

In this thesis, a thermal conductivity sensor was used to measure the CO_2 concentration of exhaled air. In doing so, two different measurement methods, the 3 omega method and the hot wire method, were tested and evaluated. Although the first intention was to utilise the 3 omega method, this could not be achieved due to the limitations of the available setup. It is feasible to enhance the measurement setup, however, this was not done as the potential improvements would have counterbalanced the advantages of a thermal conductivity sensor, which are low price and small size. It was therefore decided to use the hot wire method in steady state operation. The hot wire method achieves a sampling time of 10 ms.

A disadvantage of thermal conductivity sensors is their poor selectivity. Therefore, it is necessary to measure and compensate for humidity and temperature, as these two factors affect the measured signal. Nevertheless, by compensating for parasitic effects, it is possible to determine exhaled CO_2 within the expected range. The TC CO_2 sensor alone has a precision of $\pm 0.15\%$ CO_2. Therefore, this measurement principle has high potential for use in capnography.

By compensating for cross sensitivities, first measurements were performed. To demonstrate the functionality of this sensor principle, the effects of hyperventilation and hypoventilation were presented. Additionally, it was shown that the sensor is suitable for detecting obstructive respiratory tract alterations during illness.

The most common way to diagnose obstructive respiratory diseases is to use a spirometer. The use of a spirometer requires the supervision of a medical professional as it is not straightforward to use. It also requires forceful exhalation, which can be uncomfortable, especially for patients with an obstructive airway condition.

An alternative method for diagnosing and monitoring obstructive airway diseases is through the use of capnography. This method has the advantage of requiring only tidal breathing, making it easy to use without supervision.

By using a capnograph with a thermal conductivity sensor, it is possible to create an affordable and user-friendly device. As a capnograph is easy to use, it offers the possibility of being used as a home device. In combination with a thermal conductivity sensor, this device becomes small and affordable. Additionally, the sampling time is rapid, allowing for improved diagnosis with the additional information obtained. Thus, especially in the field of monitoring obstructive respiratory diseases, this sensor principle could offer new possibilities.

References

[1] E. Dervieux, M. Théron, and W. Uhring, "Carbon Dioxide Sensing—Biomedical Applications to Human Subjects," vol. 22, no. 1, p. 188.

[2] K. Kliche, G. Kattinger, S. Billat, L. Shen, S. Messner, and R. Zengerle, "Sensor for Thermal Gas Analysis Based on Micromachined Silicon-Microwires," vol. 13, no. 7, pp. 2626–2635.

[3] D. Zhao, D. Miller, X. Xian, F. Tsow, and E. S. Forzani, "A novel real-time carbon dioxide analyzer for health and environmental applications," vol. 195, pp. 171–176.

[4] S. Shahid, M. Geetha, K. K. Sadasivuni, D. Remani, S. Muthusamy, A. G. A. Muthalif, and S. Al-maadeed, "Highly sensitive and selective colorimetric sensing of CO2 for biomedical applications," vol. 12, no. 12, p. 334.

[5] M. Chowdhury, R. Hopper, S. Ali, J. Gardner, and F. Udrea, "MEMS Infrared Emitter and Detector for Capnography Applications," vol. 168, pp. 1204–1207.

[6] D. Berndt, J. Muggli, R. Heckel, M. F. Rahiman, M. Lindner, S. Heinrich, H. Plöchinger, and R. Schreiner, "A Robust Miniaturized Gas Sensor for H2 and CO2 Detection Based on the 3Omega Method," vol. 22, no. 2, p. 17.

[7] Z. Moussavi, "Anatomy and Physiology of Respiratory System," in *Fundamentals of Respiratory System and Sounds Analysis. Synthesis Lectures on Biomedical Engineering*, p. 8, Springer, Cham.

[8] A. Patwa and A. Shah, "Anatomy and physiology of respiratory system relevant to anaesthesia," vol. 59, no. 9, p. 533.

[9] D. Patel, K. Sharma, C. S. Chauhan, and G. Jadon, "An Overview on Respiratory System,"

[10] J. Tu, K. Inthavong, and G. Ahmadi, "The human respiratory system," in *Computational Fluid and Particle Dynamics in the Human Respiratory System*, pp. 19–44, Springer Netherlands.

[11] P. D. Wagner, "The physiological basis of pulmonary gas exchange: Implications for clinical interpretation of arterial blood gases," vol. 45, no. 1, pp. 227–243.

[12] W. F. Boron, "ORGANIZATION OF THE RESPIRATORY SYSTEM," in *Medical Physiology*, pp. 613–629, Elsevier.

[13] R. F. Schmidt and F. Lang, eds., *Physiologie des Menschen: mit Pathophysiologie*. Springer-Lehrbuch, Springer Berlin Heidelberg.

[14] J. Petersson and R. W. Glenny, "Gas exchange and ventilation–perfusion relationships in the lung," vol. 44, no. 4, pp. 1023–1041.

[15] G. Mathur, "Use of Partial Recirculation to Limit Build-Up of Cabin Carbon Dioxide Concentrations to Safe Limits per ASHRAE Standard-62," pp. 2020–01–1245.

[16] E. Mansour, R. Vishinkin, S. Rihet, W. Saliba, F. Fish, P. Sarfati, and H. Haick, "Measurement of temperature and relative humidity in exhaled breath," vol. 304, p. 127371.

[17] M. B. Jaffe, "Carbon dioxide measurement," in *Capnography* (J. S. Gravenstein, M. B. Jaffe, N. Gravenstein, and D. A. Paulus, eds.), pp. 381–396, Cambridge University Press, 2 ed.

[18] J. D'Mello and M. Butani, "CAPNOGRAPHY," vol. 46, no. 2, pp. 269–278.

[19] G. Schmalisch, "Current methodological and technical limitations of time and volumetric capnography in newborns," vol. 15, no. 1, p. 104.

[20] B. S. Kodali, "Capnography Outside the Operating Rooms," vol. 118, no. 1, pp. 192–201.

[21] I. Kerslake and F. Kelly, "Uses of capnography in the critical care unit," vol. 17, no. 5, pp. 178–183.

[22] B. Long, A. Koyfman, and M. A. Vivirito, "Capnography in the Emergency Department: A Review of Uses, Waveforms, and Limitations," vol. 53, no. 6, pp. 829–842.

[23] D. E. Supkis, "Technical specifications and standards," in *Capnography* (J. S. Gravenstein, M. B. Jaffe, N. Gravenstein, and D. A. Paulus, eds.), pp. 373–380, Cambridge University Press, 2 ed.

[24] R. K. Jha, "Non-Dispersive Infrared Gas Sensing Technology: A Review," vol. 22, no. 1, pp. 6–15.

[25] S. Essing, G. Schrag, and D. Tumpold, "Simulating Miniaturized Open Photoacoustic Gas Sensors," VDE Verlag GmbH.

[26] J. Huber, C. Weber, A. Eberhardt, and J. Wöllenstein, "Photoacoustic CO2-Sensor for Automotive Applications," vol. 168, pp. 3–6.

[27] J. B. West and P. D. Wagner, "Pulmonary Gas Exchange," vol. 157.

[28] Z. Yang, Z. Ren, Y. Cheng, W. Sun, Z. Xi, W. Jia, G. Li, Y. Wang, M. Guo, and D. Li, "Review and prospect on portable mass spectrometer for recent applications," vol. 199, p. 110889.

[29] E. L. W. Gardner, J. W. Gardner, and F. Udrea, "Micromachined Thermal Gas Sensors—A Review," vol. 23, no. 2, p. 681.

[30] S. Kommandur, A. Mahdavifar, P. J. Hesketh, and S. Yee, "A microbridge heater for low power gas sensing based on the 3-Omega technique," vol. 233, p. 22.

[31] A. Mahdavifar, M. Navaei, P. J. Hesketh, M. Findlay, J. R. Stetter, and G. W. Hunter, "Transient thermal response of micro-thermal conductivity detector (µTCD) for the identification of gas mixtures: An ultra-fast and low power method," vol. 1, no. 1, p. 15025.

[32] N. Burger, A. Laachachi, M. Ferriol, M. Lutz, V. Toniazzo, and D. Ruch, "Review of thermal conductivity in composites: Mechanisms, parameters and theory," vol. 61, pp. 1–28.

[33] R. B. Bird, W. E. Stewart, and E. N. Lightfoot, *Transport Phenomena*. Wiley, 2. ed., [nachdr.] ed.

[34] A. N. Salazar, "On thermal diffusivity," vol. 24, no. 4, pp. 351–358.

[35] D. Berndt, J. Muggli, F. Wittwer, C. Langer, S. Heinrich, T. Knittel, and R. Schreiner, "MEMS-based thermal conductivity sensor for hydrogen gas detection in automotive applications," vol. 305, p. 111670.

[36] F. Kühnel, C. Metzke, J. Weber, J. Schätz, G. S. Duesberg, and G. Benstetter, "Investigation of Heater Structures for Thermal Conductivity Measurements of SiO2 and Al2O3 Thin Films Using the 3-Omega Method," vol. 12, no. 11, p. 1928.

[37] C. Xing, C. Jensen, T. Munro, B. White, H. Ban, and M. Chirtoc, "Thermal property characterization of fine fibers by the 3-omega technique," vol. 71, no. 1, pp. 589–595.

[38] S. M. S, "Bedienungsanleitungen - monitor schiller physiogard mb 910."

[39] G. E. G. G. S. GmbH, "Bedienungsanleitungen - Defibrillator GS Elektromedizinische Geräte GmbH Corpuls3."

[40] a. T. C. c. Measurement Specialties, Inc., "MS5803-14BA Miniature 14 bar Module."

[41] S. AG, "Datasheet SHT21."

[42] S. AG, "Datasheet - SHT4x."

[43] R. J. Scheenstra, S. H. Muller, A. Vincent, A. H. Ackerstaff, I. Jacobi, and F. J. Hilgers, "A New Heat And Moisture Exchanger for Laryngectomized Patients: Endotracheal Temperature and Humidity," vol. 56, no. 5, pp. 604–611.

[44] U. Mogera, A. A. Sagade, S. J. George, and G. U. Kulkarni, "Ultrafast response humidity sensor using supramolecular nanofibre and its application in monitoring breath humidity and flow," vol. 4, no. 1, p. 4103.

[45] H. R. Genderingen, N. Gravenstein, J. J. Aa, and J. S. Gravenstein, "Computer-assisted capnogram analysis," vol. 3, no. 3, pp. 194–200.

[46] C. L. Herry, D. Townsend, G. C. Green, A. Bravi, and A. J. E. Seely, "Segmentation and classification of capnograms: Application in respiratory variability analysis," vol. 35, no. 12, pp. 2343–2358.

[47] L. Talker, D. Neville, L. Wiffen, A. B. Selim, M. Haines, J. C. Carter, H. Broomfield, R. H. Lim, G. Lambert, BRS Study Team, J. Winter, A. Gribbin, M. Chauhan, R. De Vos, P. Kalra, S. Begum, B. Robinson, B. Mundy, H. Rutter, K. Madronal, S. T. Weiss, G. Hayward, T. Brown, A. Chauhan, and A. X. Patel, "Machine diagnosis of chronic obstructive pulmonary disease using a novel fast-response capnometer," vol. 24, no. 1, p. 150.